# Improving Urban Climate Adaptation Modelling in the Community Earth System Model (CESM) Through Transient Urban Surface Albedo Representation

**Yuan Sun[1,2], Bowen Fang[3], Keith W. Oleson[4], Lei Zhao[3,5,6], David O. Topping[1], David M. Schultz[1,2], Zhonghua Zheng[1,2]**

[1]Department of Earth and Environmental Sciences, The University of Manchester, Manchester M13 9PL, UK
[2]Centre for Crisis Studies and Mitigation, The University of Manchester, Oxford Road, Manchester, M13 9PL, UK
[3]Department of Civil and Environmental Engineering, University of Illinois Urbana-Champaign, Urbana, IL 61801, USA
[4]Climate and Global Dynamics Laboratory, National Center for Atmospheric Research, Boulder, CO 80307, USA
[5]National Center for Supercomputing Applications, University of Illinois Urbana-Champaign, Urbana, IL 61801, USA
[6]Institute for Sustainability, Energy, and Environment (iSEE), University of Illinois Urbana-Champaign, Urbana, IL 61801, USA

## Statement

This manuscript is a preprint submitted to *EarthArXiv* and will be shortly submitted for publication to a scientific journal. As a function of the peer-reviewing process that this manuscript will undergo, its structure and content may change.

If accepted, the final version of this manuscript will be available via the 'Peer-reviewed Publication DOI' link on the right-hand side of this webpage. Please feel free to contact any of the authors; we welcome feedback.

**Key Points:**

- We developed a new representation scheme of transient urban surface albedo in CESM to improve urban climate adaptation modelling.
- The new scheme enables CESM to assess evolving adaptation strategies for roofs, impervious roads, and walls over time.
- Simulations show increasing roof albedo cools cities more effectively than increasing wall or impervious road albedo.

Corresponding author: Yuan Sun, `yuan.sun-7@postgrad.manchester.ac.uk`

Corresponding author: Zhonghua Zheng, `zhonghua.zheng@manchester.ac.uk`

## Abstract

Increasing the albedo of urban surfaces, through strategies like white roof installations, has emerged as a promising approach for urban climate adaptation. Yet, modelling these strategies on a large scale is limited by the use of static urban surface albedo representations in the Earth system models. In this study, we developed a new transient urban surface albedo scheme in the Community Earth System Model and evaluated evolving adaptation strategies under varying urban surface albedo configurations. Our simulations model a gradual increase in the urban surface albedo of roofs, impervious roads, and walls from 2015 to 2099 under the SSP3-7.0 scenario. Results highlight the cooling effects of roof albedo modifications, which reduce the annual mean canopy urban heat island from 0.8°C in 2015 to 0.2°C by 2099. Compared to high-density and mid-density areas, higher albedo configurations are more effective in cooling environments within tall building districts. Additionally, urban surface albedo changes lead to changes in building energy consumption, where high albedo results in more indoor heating usage in urban areas located beyond 30°N and 25°S. The scheme developed in this study offers potential for non-policy applications, like simulating natural albedo variations across urban surfaces, and enables the inclusion of other urban canopy parameters, such as surface emissivity.



## Plain Language Summary

Higher albedo surfaces reflect more sunlight, which helps cool down cities. Yet, research into how altering the albedo of urban surfaces on a global scale can aid climate adaptation is limited. It either relies on empirical analysis, oversimplifying urban physical processes, or assumes that urban surface albedo remains constant over time. These limitations hinder our understanding of how changes in urban surfaces can impact the urban thermal environment. In this study, we developed a new option that allows urban surface albedo to vary over time within a global climate model and quantified the cooling effects of increasing surface albedo in global urban areas. This new option sets the stage for future exploration of scenarios like painting roofs white or how materials age, shedding light on effective urban climate adaptation strategies.


## 1 Introduction

Urban areas are often hotter than their surroundings and are increasingly vulnerable to extreme heat events (e.g. Krayenhoff et al., 2021; Tuholske et al., 2021; Zhao et al., 2014, 2021; Zheng et al., 2021). The escalating urban heat stress necessitates the need for effective cooling strategies as part of urban climate adaptation efforts (Djukic et al., 2016; Dursun & Yavas, 2015). Improving the urban thermal environment has become a focal point, with efforts to alter the built-up layout (e.g. Jamei et al., 2019; Zeng et al., 2023), morphological form (e.g. Liao et al., 2021), and biophysical properties, including surface roughness (e.g. Hou et al., 2023), emissivity (e.g. Chakraborty et al., 2021), and albedo (e.g. Liu et al., 2024). Among the array of adaptation strategies, using highly-reflective materials (Chen et al., 2019; Santamouris et al., 2011) and modifying coating color and texture (Senevirathne et al., 2021) have proven to be particularly effective. These strategies, focusing on altering the surface albedo of urban roofs and pavements (Yang et al., 2015), reduce temperatures and mitigate urban heat island effects.

The albedo of urban surfaces refers to the capacity of these surfaces to reflect or absorb solar radiation, influencing local heat conditions by determining the amount of solar radiation absorbed. To assess the cooling effects of managing urban surface albedo, a variety of methods have been developed, including statistical estimations (Akbari et al., 2009; Boriboonsomsin & Reza, 2007; Santamouris & Fiorito, 2021), physical-based experimentations (Lopez-Cabeza et al., 2022; Salvati et al., 2022), and multi-scale numerical simulations (Krayenhoff et al., 2021). These investigations mainly focus on meso or micro-scale built environments, providing scientific evidence of changing albedo to deal with urban heat issues in certain cities. Besides concerning regional urban albedo effects, there is an emerging trend of implementing high albedo cross regions, gradually shaping international networks such as C40 cities (`https://www.c40.org/`) for urban climate adaptation. So far, it remains challenging to quantify urban albedo impacts at a larger scale. Akbari et al. (2009) revealed that increasing horizontal surface albedo by 0.01 could increase global solar reflection by 1.27 W m$^{-2}$ and achieve an equivalency of 1.4 kg m$^{-2}$ $CO_2$ offset in urban areas. Xu et al. (2020) introduced that $CO_2$ equivalency by 0.01 pavement albedo changes ranges from 0.8 to 1.6 kg m$^{-2}$ when specifying meteorological attributes in fourteen U.S. cities. However, these empirical studies are based on stationary climate conditions and oversimplify urban physical processes. To explicitly represent urban physical processes, several studies (Tab.1) have employed process-based global climate models (GCMs) or Earth System Models (ESMs) to quantify albedo impacts under climate-change scenarios, such as the Community Earth System Model (CESM) (Oleson et al., 2010; Zhang et al., 2016; Zhao et al., 2017), the University of Victoria Earth System Climate Model (UVic ESCM) (Akbari & Matthews, 2012; Akbari et al., 2012), and the global-regional Gas, Aerosol, Transport, Radiation, General Circulation, Mesoscale, and Ocean Model (GATOR-GCMOM) (Jacobson & Ten Hoeve, 2012). By simulating urban albedo-induced changes in different periods, these studies provided scientific evidence for urban climate adaptation strategies. For instance, using the Community Land Model-Urban (CLMU), Oleson et al. (2010) demonstrated that installing white roofs (with a roof albedo of 0.9) across urban areas worldwide could result in a 33% decrease in the annual mean canopy urban heat island (CUHI) intensity. Additionally, through atmosphere–land coupled simulations, Zhang et al. (2016) found that the impacts of 'cool roofs' (also with a roof albedo of 0.9) on global climate are statistically insignificant.

Although studies using GCMs/ESMs explore the effects of high urban surface albedo, they fall short of adequately informing urban climate adaptation efforts. It is important to note that the fidelity of urban climate projections within these models is influenced by the representation and parameterization of urban areas (e.g., urban areas are much smaller than the grid-box size in the global models). Notably, most GCMs/ESMs bypass detailed urban modelling (Zhao et al., 2021; Zheng et al., 2021). For GCMs/ESMs with urban models incorporated, the heterogeneity and complexity of urban density classes and surfaces are often simplified (Hertwig et al., 2021). Such simplification can introduce biases in urban climate simulations, consequently affecting the evaluation of adaptation strategies' effectiveness. For instance, simulations using the Catchment Land Surface Model (CLSM) with a high urban albedo value, where urban surfaces were not explicitly resolved, demonstrate a lack of resolution independence in their outputs of total radiation values (Menon et al., 2010). Moreover, these studies apply static albedo parameters for simulations (Oleson et al., 2010; Zhang et al., 2016), not considering any implementation schedule for urban albedo changes. For instance, implementing high-albedo measures such as white-roof installations in urban areas is a gradual process, unlikely to be completed within a single day. Recognizing the dynamic nature of urban albedo changes is crucial for assessing the impact of such adaptations on urban climate resilience and planning effective strategies to mitigate urban heat island effects. This study leverages the state-of-the-art Earth system model, CESM, to simulate the phased introduction of high-albedo interventions in urban environments. We realize modelling the gradual adoption of urban high-albedo strategies and quantify their effects.

This paper is organized as follows. In Sec. 2, we outline CESM's urban representation and parameterization, highlighting our development of a transient urban albedo scheme. This new scheme is introduced as an alternative to the default scheme of static urban surface albedo. Sec. 3 presents the simulation results of continuously increasing albedo. Output analysis involves quantifying urban heat mitigation, urban surface energy changes, and urban land unit and surface heterogeneity. Sec. 4 delves into the im-

**Table 1.** Literature on quantifying effects of high surface albedo in large-scale climate models.

| Reference | Global climate model | Component set | Atmospheric forcing | Simulation period | Simulation domain and grid spacing | Urban representation | Urban albedo changes | Effect quantification |
|---|---|---|---|---|---|---|---|---|
| Oleson et al. (2010) | Community Climate System Model (CCSM) | Atmosphere–land coupled | Qian et al. (2006) | 1941–1999 | Global, 1.9° latitude by 2.5° longitude | Explicit at the subgrid level: roof, wall and road | A step change in roof albedo from 0.32 to 0.9 | Canopy urban heat island (−33%), daily maximum temperature (−0.6°C), minimum temperature (−0.3°C) |
| Menon et al. (2010) | Goddard Earth Observing System Model Version 5 (GEOS-5) | Land-only | GSWP-2 data (Dirmeyer et al., 2006) | 1984–1995 | Global, 2° latitude by 2.5° longitude; continental US, 0.5° latitude by 0.5° longitude | Inexplicit: 0.7% of global surface areas | Step changes in roof albedo by 0.25 and pavement albedo by 0.15 | Global radiation forcing (1.63 W $m^{-2}$), emitted $CO_2$ offset (57Gt) |
| Akbari and Matthews (2012) | University of Victoria Earth System Climate Model (UVic ESCM) | Fully coupled | Atmospheric model outputs | 1800–2200 | Unknown | Inexplicit: 1% of global surface areas | Step changes in land surface albedo by 0.05 and 0.1, respectively | Land surface temperature(−1.5 and −3K in 2200, respectively), emitted $CO_2$ offset (160Gt in 2200) |
| Akbari et al. (2012) | UVic ESCM | Fully coupled | Atmospheric model outputs | 2010–2300 | Unknown | Explicit at the grid level: urban areas | A step change in urban albedo by 0.1 | Atmospheric temperature (−0.01-0.07°C), emitted $CO_2$ offset (25-150Gt) |
| Jacobson and Ten Hoeve (2012) | Gas, Aerosol, Transport, Radiation, General Circulation, Mesoscale, and Ocean Model (GATOR-GCMOM) | Fully coupled | Atmospheric model outputs | 20 years | Global, 4° latitude by 5° longitude | Explicit at the grid level: roof and wall | A step change in roof albedo from 0.12 to 0.65 | Land air temperature (0.07°C), urban air temperature(−0.02°C) |
| Zhang et al. (2016) | Community Earth System Model (CESM) | Atmosphere–land coupled | Common Atmosphere Model (CAM) outputs | 2010–2039 | Global, 1.9° latitude by 2.5° longitude | Explicit at the subgrid level: roof, wall and road | A step change in roof albedo from 0.15 to 0.9 | Canopy urban heat island reduction (−0.4°C) |
| Zhao et al. (2017) | CESM | Land-only | Data CAM outputs from fully coupled simulations | 2071–2100 | US and southern Canada, 1.9° latitude by 2.5° longitude | Explicit at subgrid level: roof, wall and road | A step change in roof albedo increase to 0.88 | Surface urban heat island (−3.4°C) |

Note: Atmosphere–land coupled set refers to a configuration in GCMs/ESMs where both the atmosphere and land components are active. Land-only set denotes that only the land component is active, with forcings from atmosphere data. Fully coupled set denotes a configuration where at least the ocean, atmosphere, and land components are active.

plications of our findings for urban climate-sensitive design, focusing on seasonal variations, spatial differences, and effects specific to different latitudes. Finally, Sec. 5 provides a summary of our conclusions and insights.

## 2 Methods and data

This section describes the urban model in CESM (Sec. 2.1) and the new transient urban albedo scheme (Sec. 2.2). To examine the time-varying albedo functionality, we performed a series of simulations that vary urban albedo configuration (Sec. 2.3) with the corresponding model inputs (Sec. 2.4). We quantified albedo-induced changes based on the CESM simulations (Sec. 2.5).

### 2.1 Urban representation and parameterization

The land component of CESM, known as the Community Land Model (CLM) (Lawrence et al., 2019), represents urban areas using a subgrid approach. The urban parameterization of CLM (CLMU), developed by Oleson et al. (2013), allows simulations of urban climate. In essence, CLMU classifies urban areas into density classes–tall building district (TBD), high density (HD), and medium density (MD)–and adopts Oke (1987) 'urban canyon' concept. The 'urban canyon' delineates urban landunits into five surfaces: roof, sunlit wall, shaded wall, impervious and pervious canyon floor. The CLMU technical description can be found in Oleson et al. (2013), with Figure A1 illustrating the CLM's representation hierarchy, the urban feedback to atmospheric model, and the conceptualization of urban canyons and urban energy dynamics.

The single-layer urban canopy model of CLMU accounts for biophysical interactions between the atmosphere and urban canyon, where several biogeophysical modules calculate heat and water fluxes on each urban surface (`https://github.com/ESCOMP/CTSM/tree/master/src`). The albedo of each urban surface directly affects reflected and absorbed solar radiation (see CESM source code file 'UrbanAlbedoMod.F90'), with secondary effects on longwave and turbulent fluxes, and canyon air temperature. For instance, walls are distinguished as sun-walls and shade-walls with their individual radiative properties (Masson, 2000). Additionally, CLM5 integrates anthropogenic factors by incorporating a building energy model(Oleson & Feddema, 2020; Wang et al., 2023). This addition facilitates the simulation of indoor thermal conditions and heat exchanges, crucial for calculating the anthropogenic heat flux due to space heating and air conditioning.

In a CESM simulation, the initialization process starts with the 'UrbanParameType' module (Figure 1), which reads urban constant parameters from the land surface input data. These include eight urban albedo parameters: diffuse albedo and direct albedo for roof, wall, impervious road, and pervious road. Each albedo parameter is defined by four dimensions: the number of solar bands ('numrad'), the number of urban density types ('numurbl'), the latitude ('lsmlat') and the longitude ('lsmlon'). That is, urban albedo parameters are spilt out into direct and diffuse albedos with visible and near-infrared wave bands. Once initialized, these parameters remain unchanged throughout the simulation. Thus, under the default scheme, modifying urban surface parameters such as albedo requires pausing the simulation, updating land surface data files, and initiating a new branch case. This method, aimed at representing transient urban surface parameters, interrupts the workflow with interim outputs and results in extra time spent on output archiving, waiting in job queues, and the restarting process.

### 2.2 Implementation of the transient urban albedo scheme

We developed the 'UrbanDynAlbMod', a new module within CLM5, specifically designed for the transient urban albedo scheme (Figure 1). This module allows for dynamic modification of urban albedo parameters by adding a temporal dimension, permitting users to delineate albedo changes over specific time intervals, ranging from seconds to years. Focused on built surfaces–roofs, walls, and impervious roads–this scheme intentionally excludes pervious surfaces like urban residential lawns and parks to maintain their natural characteristics, as detailed by Oleson and Feddema (2020).

The scheme provides three configurable options: '`Dynamic_UrbanAlbedoRoof`', '`Dynamic_UrbanAlbedoImproad`', and '`Dynamic_UrbanAlbedoWall`'. Users can tailor urban albedo modifications to their needs by enabling any of these options in the CLM name list. For instance, activating '`Dynamic_UrbanAlbedoWall=.true.`' triggers the UrbanDynAlbMod, which then processes input data streams for variables such as `DYN_ALBEDO_WALL_TBD`, `DYN_ALBEDO_WALL_HD`, and `DYN_ALBEDO_WALL_MD`. These variables are defined across three dimensions: time, 'lsmlat', and 'lsmlon', ensuring consistency in both diffuse and direct albedo values across the solar bands ('numrad'), similar to the handling of default constant parameters. The 'UrbanDynAlbMod' then seamlessly incorporates these transient albedo parameters into the 'UrbanAlbedoMod' for the computation of radiation and turbulent fluxes.

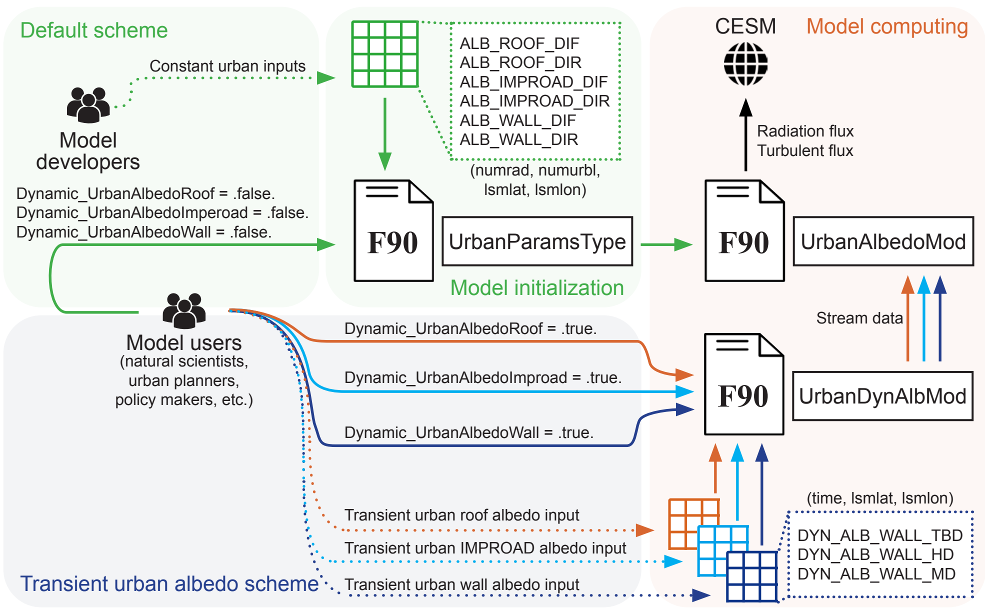


**Figure 1.** Workflow for implementing user-customized transient urban albedo. In the 'UrbanParamsType' input data, the 'numrad' dimension refers to the number of solar bands, encompassing both visible and near-infrared bands. The 'numurbl' dimension refers to the number of urban density classes: TBD, HD, and MD. Dimensions 'lsmlat' and 'lsmlon' are land-masked latitude and longitude, respectively. For 'UrbanDynAlbMod', the input data's 'time' dimension signifies annual time steps for albedo modifications, complemented by 'lsmlat' and 'lsmlon' dimensions.

### 2.3 Experimental design

We used CESM2.1.4 to assess urban climate adaptation strategies under varying urban albedo configurations with a grid spacing of 0.9° latitude by 1.25° longitude (Tab. 2). We executed CESM in a 'land-only' mode with an active CLM5, forced by atmospheric data. Simulations started with a 50-year spin-up driven by the satellite phenology (Li et al., 2022). After spin-up, the model reached a steady state, indicated by the evidence that urban sensible heat flux and latent heat flux during the last 10 years were stable around 55.96±0.38 and 35.45±0.30 W $m^{-2}$, respectively. Then, simulations ran over 85 years from 2015 to 2099 in the Shared Socioeconomic Pathways (SSPs) scenario SSP3-7.0 (Riahi et al., 2017). The SSP3-7.0 scenario outlines a future where limited action is taken to mitigate climate change or adapt to its impacts, leading to steadily increasing emissions and temperatures. This pathway projects CO2 emissions to approximately double from current levels by 2100. Atmospheric forcing in this future scenario came from existing fully coupled simulations conducted by the National Center for Atmospheric Research (NCAR), based on the 'BSSP370cmip6' (`SSP370_CAM60_CLM50%BGC-CROP-CMIP6DECK_CICE%CMIP6_POP2%ECO%ABIO-DIC_MOSART_CISM2%NOEVOLVE_WW3_BGC%BDRD`) components set. Note the simulations from NCAR were submitted to the Coupled Model Intercomparison Project Phase 6 (CMIP6) for IPCC assessment. Additionally, this study did not consider urban land changes in the SSP3-7.0 scenario (Gao & O'Neill, 2020).

The control simulation (CNTL) acted as the baseline for comparison. The ROOF_0.9 simulation applied a static roof albedo of 0.9, emulating the maximum reflectivity of a white roof. Note both CNTL and ROOF_0.9 used the default scheme with static input data, aiming to replicate earlier studies by Oleson et al. (2010) and Zhang et al. (2016). In contrast, the ROOF_DA simulation used the transient urban albedo scheme, incrementally increasing roof albedo by 0.01 (Akbari et al., 2012) annually since 2015, until reaching a maximum of 0.9, after which no further increases occurred. Similarly, the IMPROAD_DA and WALL_DA simulations implemented annual increases in impervious road albedo and wall albedos, respectively. The combined impacts of albedo modifications were further examined in ROOF_IMPROAD_DA and ROOF_IMPROAD_WALL_DA simulations, offering insights into the synergistic effects of varying albedo modifications on urban climate adaptation. The annual increment of 0.01 in the albedo of specific urban surfaces is an experimental assumption to model interventions. For example, in the ROOF_DA simulation, a 0.01 roof albedo increase per year raises the global mean urban surface albedo by 0.0044 per year, based on the assumption that roofs account for 44% of the urban surface. This rate is ten times as high as the real-world urban surface albedo changes observed (0.0044 per decade) in 11 Chinese cities from 1986 to 2018 (Guo et al., 2022), which was attributed to multiple human activities including urban greening and conversion of natural surfaces into bright or dark built-up areas. In reality, the trend of global urban albedo changes is modest and generally downward. Ouyang et al. (2022) reported decreasing urban surface albedo alongside urbanization by converting croplands into urban lands. Wu et al. (2024) found that the downward urban albedo accelerated in recent decades, given that the annual-mean city-level albedo decreased rate during 2000-2020 was 0.0014 per year, twice as high as during 1986–2020. Compared to real-world observations, our assumptions of a 0.01 albedo increase rate on certain surfaces are far higher than the status quo, supposing intentional adaptation actions such as installing white roofs and applying high-reflective materials to accelerate urban albedo increase.

**Table 2.** Urban climate adaptation strategies under varying urban albedo configurations.

| Simulation name | Input data description | Roof albedo | Wall albedo | Impervious road albedo | Pervious surface albedo |
|---|---|---|---|---|---|
| CNTL | Static urban albedo | □ | □ | □ | □ |
| ROOF_0.9 | Static high albedo of roof | 0.9 | □ | □ | □ |
| ROOF_DA | Transient albedo of roof | ■ | □ | □ | □ |
| WALL_DA | Transient albedo of wall | □ | ■ | □ | □ |
| IMPROAD_DA | Transient albedo of impervious road | □ | □ | ■ | □ |
| ROOF_IMPROAD_DA | Transient albedo of horizontal built surfaces | ■ | □ | ■ | □ |
| ROOF_IMPROAD_WALL_DA | Transient albedo of vertical and horizontal built surfaces | ■ | ■ | ■ | □ |

Note: The symbol □ represents static urban albedo parameters in CLM5, while ■ is transient urban surface albedo inputs. Albedo values in each grid cell were modified to increase annually by 0.01 starting from 2015, capping at a maximum of 0.9. The albedo of pervious roads was not altered, in recognition of their natural characteristics.

### 2.4 Land surface input data

The default input data for urban land cover and urban canopy parameters in CLMU are derived from the Jackson et al. (2010). The urban fractions are represented through the parameter PCT_URBAN (percent urban for each density type). As illustrated in Figure 2(a)–(c), the majority of urban areas, accounting for 79.01%, are classified as MD, while TBD and HD areas represent 0.1% and 20.89%, respectively. The PCT_URBAN parameters are static, without considering urbanization-induced changes in urban areas. Based on a categorization of global urban regions, Jackson et al. (2010) developed a set of constant global urban morphological, radiative, and thermal parameters for CLMU. The default configuration in CLMU standardizes albedo values for both direct and diffuse reflectance, maintaining consistent behaviour across both visible and near-infrared bands. Figure 2 (d)–(f), illustrates the categorization of urban roof albedo constants in the default input dataset, spanning 33 urban regions with three distinct urban density types.

Alongside the default input dataset, a series of datasets featuring transient urban albedo values have been developed, each corresponding to the simulations outlined in Tab.2. These datasets follow a hypothetical scenario where albedo is incrementally increased by 0.01 each year, reaching a cap of 0.9 (see Sec. 2.3).

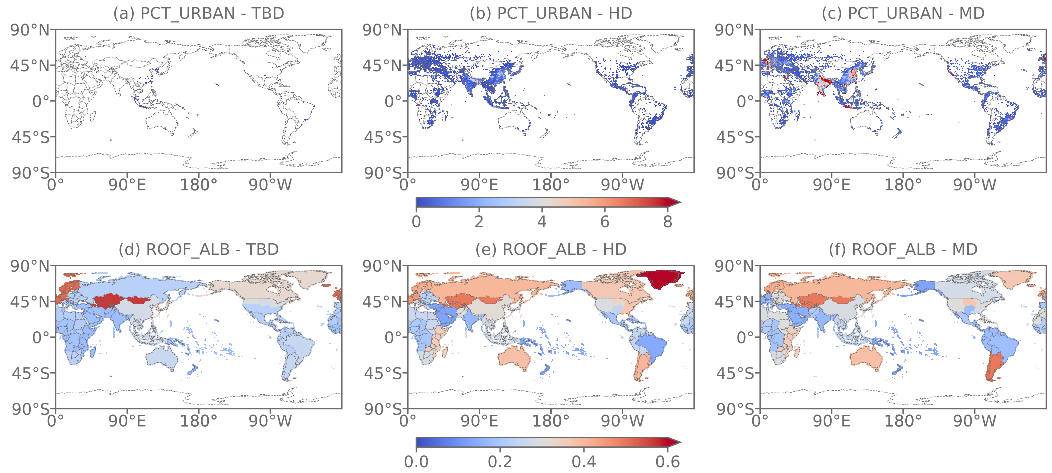


**Figure 2.** Spatial variation of urban fraction (%) and static roof albedo in the standard CESM land surface input data. (a), (b), (c) Percent of urban areas (%) in TBD, HD, and MD. (d), (e), (f) Roof albedo in TBD, HD, and MD. Both parameters come from raw data aggregated to 0.05° resolution (Oleson & Feddema, 2020).

### 2.5 Analysis of effects induced by urban surface albedo modifications

Previous studies have focused on the albedo cooling effects on urban surface temperature, 2-m air temperature, and indoor temperature, with further analysis on urban heat island intensity and the possibility of reducing air conditioning needs (Yang et al., 2015). The potential drawbacks of increased urban surface albedo, such as intensified thermal stress in the street canyons (Erell et al., 2014), and elevated heating demands during winter (Georgescu et al., 2014), have been acknowledged as well. Based on CESM simulations, we explored the implications for urban thermal environments, the urban energy budget, and urban land unit and surface heterogeneity. Our analysis spans three future periods as outlined by the Intergovernmental Panel on Climate Change (IPCC) (2023): the near-term (2021–2040), mid-term (2041–2060), and long-term (2081–2099), providing an insight into the impacts of urban albedo modifications.

#### *2.5.1 Urban thermal environments*

Urban thermal environments are assessed through several temperature indices, including global-mean urban heat island intensity, urban heat stress, and indoor air temperature (Sec. 3.1). Urban heat island is calculated by contrasting urban and rural temperatures, involving land surface temperature for surface urban heat island (SUHI) intensity and 2-meter near-surface air temperature for canopy urban heat island (CUHI) intensity. The SUHI and CUHI intensity are calculated by:

$$\mathrm{SUHI} = \mathrm{TG\_U} - \mathrm{TG\_R}, \tag{1}$$

and

$$\mathrm{CUHI} = \mathrm{TSA\_U} - \mathrm{TSA\_R}, \tag{2}$$

where TG_U and TG_R are the surface temperatures in urban and rural areas, respectively, and TSA_U and TSA_R are the 2-m air temperatures in the urban and rural areas, respectively. TSA_R and TG_R come from fraction-weighted corresponding variables in vegetated and crop fractions. Urban heat stress is assessed by a set of human-related indices (Oleson et al., 2015), including the 2-m US National Weather Service Heat Index (NWS_HI) (Steadman, 1979), 2-m apparent temperature (AT) (Steadman, 1994), 2-m simplified wet-bulb globe temperature (SWBGT) (Willett & Sherwood, 2012), 2-m humidity index (HUMIDEX) (Masterton & Richardson, 1979), and 2-m discomfort index (DI) (Epstein & Moran, 2006). These urban heat stress metrics were obtained from the human index module named HumanIndexMod in CLM5 (Buzan et al., 2015), defined by:

$$\begin{aligned}\mathrm{NWS\_HI} = &- 42.379 + 2.049 \times T_f + 10.143 \times \mathrm{RH} - 0.224 \times T_f \times \mathrm{RH} \\ &- 6.838 \times 10^{-3} \times T_f^2 - 5.482 \times 10^{-2} \times \mathrm{RH}^2 \\ &+ 1.229 \times 10^{-3} \times T_f^2 \times \mathrm{RH} \\ &+ 8.528 \times 10^{-4} \times T_f \times \mathrm{RH}^2 - 1.99 \times 10^{-6} \times T_f^2 \times \mathrm{RH}^2,\end{aligned} \tag{3}$$

$$\mathrm{AT} = T_c + 3.30 \times V_p/1000 - 0.70 \times U_{10} - 4.0, \tag{4}$$

$$\mathrm{SWBGT} = 0.567 \times T_c + 0.393 \times V_p/100 + 3.94, \tag{5}$$

$$\mathrm{HUMIDEX} = T_c + \frac{5}{9}(V_p/100 - 10), \tag{6}$$

and

$$\mathrm{DI} = 0.5 \times W_t + 0.5 \times T_c, \tag{7}$$

where $T_f$ is the air temperature in Fahrenheit (°F), RH is the relative humidity (%), $T_c$ is the air temperature (°C), $V_p$ is the vapour pressure (Pa), $U_{10}$ is the 10-m winds (m $\mathrm{s}^{-1}$), $W_t$ is the 2-m wet-bulb temperature (°C) calculated by using Stull (2011) method.

#### *2.5.2 The urban surface energy budget*

We used regression analysis to identify the impacts of roof albedo modification on urban energy fluxes (Sec. 3.2), using the surface energy balance introduced in CLMU as:

$$\mathrm{FSA} - \mathrm{FIRA} = \mathrm{FSH} + \mathrm{FLH} + (\mathrm{FGR} - \mathrm{AC} + \mathrm{HEAT}) - \mathrm{WASTEHEAT} - \mathrm{HEAT}, \tag{8}$$

where FSA is the urban absorbed solar radiation (W $\mathrm{m}^{-2}$), FIRA is the urban net longwave radiation, FSH is the urban sensible heat, FLH is the urban total latent heat, FGR is the urban heat flux into soil/snow, which includes the heating and cooling flux, WASTEHEAT is the sensible heat flux from heating and cooling sources of urban waste heat, AC is the sensible heat flux put into the street canyon due to heat removed from air conditioning, and HEAT is the urban heat flux. Both AC and HEAT are calculated based on TBUILD without considering socio-economical factors (Biardeau et al., 2020). Specifically, there is a minimum indoor temperature as the threshold of heating in every grid cell and CLMU calculates HEAT when the indoor temperature is below the minimum. Similarly, CLMU calculates AC when the indoor temperature is higher than the maximum. Accordingly, the anthropogenic heat flux (AHF) to the climate system is modelled as comprising urban heating flux and sensible heat from both urban heating and air-conditioning waste heat, while excluding other heat sources like urban traffic and human metabolism due to a lack of suitable global data:

$$\mathrm{AHF} = \mathrm{HEAT} + \mathrm{WASTEHEAT}. \tag{9}$$

To examine how absorbed solar radiation would change by albedo increases under the SSP3-7.0 scenario, we conducted the statistical regression using the fixed effects model. In all simulations, both urban surface albedo and FSDS (Figure C1) are transient under the SSP3-7.0 scenario, thereby considered as independent variables in the regression model. We introduce a dummy variable $\mu_g$ to fix entity (grid cell) specific effects. That is, grid cells sharing the same urban albedo might have different performances of reflecting or absorbing solar radiation, given their specific land-unit structure, morphological characters and thermal properties. Fixing entity effects aimed to omit underlying factors within certain urban areas. The regression model is expressed as:

$$\mathrm{FSA}_{t,g} = \beta_1 \times \mathrm{ALB}_{t,g} + \beta_2 \times \mathrm{FSDS}_{t,g} + \mu_g, \tag{10}$$

where $\mathrm{FSA}_{t,g}$ is the absorbed solar radiation of a certain grid $g$ at a certain time of $t$, $\beta$ is the coefficient of the independent variable, $\mathrm{FSDS}_{t,g}$ is the incoming shortwave radiation, and $\mathrm{ALB}_{t,g}$ is the land-unit averaged urban surface albedo, calculated by

$$\mathrm{ALB}_{t,g} = \sum^{z,u}(\mathrm{Surface}_{z,u,g} \times \alpha_{t,z,u,g}) / \sum^{z,u}\mathrm{Surface}_{z,u,g}, \tag{11}$$

where $\mathrm{Surface}_{u,g}$ is the fraction of the certain surface in the certain land unit $u$ of the grid cell ($g$), $t$ indexes the specific year (from 2015 to 2099), $z$ indexes urban surfaces (i.e. roof, impervious road, wall), and $u$ indexes urban land unit types (i.e., TBD, HD, MD). This equation is inspired by Zhang et al. (2016) but modified by additionally considering transient albedo and the land unit types.

#### *2.5.3 Urban heterogeneity and implication for design strategies*

To meet the need for fine design, we examined the albedo cooling effects within the context of urban heterogeneity (Sec. 3.3), encompassing urban density classes (TBD, HD, MD) and surfaces (roof, impervious road, and wall). We analyzed the impacts of urban albedo modifications on these urban features, taking into account their distinct unique morphological, thermal, and radiative properties. These characteristics are localized in grid cells, which leads to spatial variations across global urban areas. Besides focusing on urban temperature reduction, we assessed the implications of albedo modifications for developing urban climate-sensitive design strategies (Sec. 4). We raised particular concerns about the indoor thermal environment, with a focus on balancing energy consumption and savings by latitude.

## 3 Result and discussion

### 3.1 Continuous mitigation of urban heat with transient roof albedo

We first assessed the impacts of urban roof adaptation strategies on urban thermal environments through the CNTL, ROOF_0.9, and ROOF_DA simulations. In the CNTL simulation, without urban climate intervention, the annual-mean CUHI and SUHI stand at 0.7±0.02°C (mean±std) and 1.2±0.03°C, respectively (Figure 3). CUHI averages 0.5±0.02°C during the day and 0.9±0.02°C at night, aligning closely with the global observation data that indicates an annual-mean daytime CUHI of 0.6±1.3°C and nighttime CUHI of 0.8±1.4°C (Du et al., 2021). Seasonal patterns reveals that the mean CUHI is higher by 0.2±0.03°C in the boreal summer (JJA) than in the boreal winter (DJF).

In the ROOF_0.9 simulation, we replaced the default roof albedo values (as set in the CNTL simulation) with 0.9 across all urban areas over the globe for the entirety of the simulation period. This modification leads to a large decrease in the annual-mean CUHI from 0.7°C to 0.2°C (−0.5±0.005°C), and in the annual-mean SUHI from 1.2 to −1.5°C (−2.7±0.02°C), indicating a more pronounced response of SUHI to changes in roof surface albedo. Specifically, the reduction in mean SUHI during summer (JJA) reaches −3.0±0.04°C, exceeding the winter (DJF) mean SUHI reduction of (−2.1±0.03°C). Notably, the negative SUHI values suggest that urban surface temperatures with a roof albedo of 0.9 were even lower than those in rural areas. Comparing the CNTL and ROOF_0.9 simulation results, the 0.5°C CUHI reduction aligns with the findings by Oleson et al. (2010), which reports a decrease in annual-mean CUHI by 0.4°C (from 1.2°C to 0.8°C), as a result of increasing roof albedo from 0.32 to 0.9. The differences in annual-mean CUHI values between our study and the findings of Oleson et al. (2010) can be partly attributed to variations in simulation setups. Their study spanned from 1941 to 1999, relying on present-day atmospheric forcings, whereas our projections extended from 2015 to 2099 under the SSP3-7.0 scenario. Additionally, our land-only simulations, conducted with the Community Land Model version 5 (CLM5) coupled with an updated building energy model, differ from Oleson et al. (2010)'s atmosphere–land coupled simulations that used CLM3.5 with a coarser grid spacing of 1.9° latitude by 2.5° longitude.

In the ROOF_DA simulation, we observed an instant response of urban thermal environments to transient albedo changes, evidenced by a continuous decrease in CUHI and SUHI intensity. The reduction rate of CUHI (ΔCUHI per 0.01 increase in roof albedo) is quantified as $-0.009\pm0.0001$°C, as shown in Figure 3(a), and ΔSUHI at $-0.04\pm0.0002$°C, as shown in Figure 3(d). The continuous downward trends reflect the transient representation of albedo variables in CLMU, where the UrbanAlbedoMod module computes transient urban albedo parameters in a given year, incorporating new albedo values into each simulation time step. The annual-mean CUHI started at 0.8°C in 2015, similar to the counterpart in the CNTL simulation, and would diminish to 0.2°C by 2099, aligning with the counterpart in the ROOF_0.9 simulation. Additionally, the CUHI reduction rates during the day and night are $0.01\pm0.0001$°C and $0.005\pm0.0001$°C per year, respectively, suggesting the potential of adaptive albedo modifications in mitigating urban heat island effects.

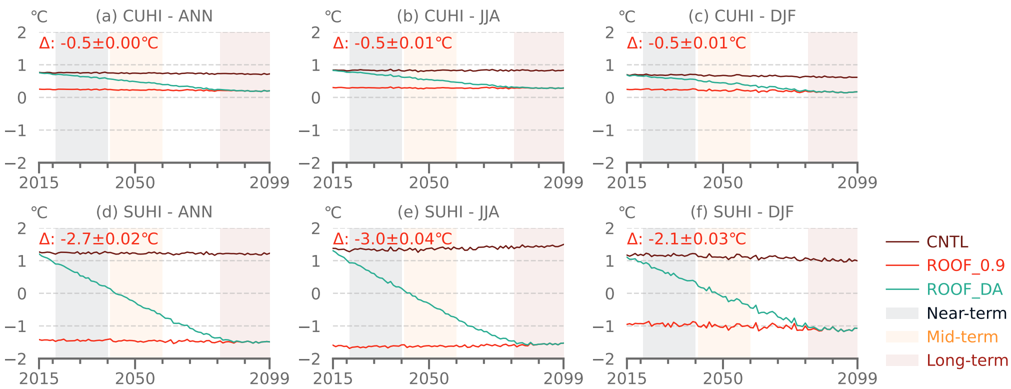


**Figure 3.** Global-mean canopy urban heat island (CUHI) intensity and surface urban heat island (SUHI) intensity during 2015-2099 in the CNTL, ROOF_0.9, and ROOF_DA simulations. Δ denotes the reductions of global-mean±std urban temperature by ROOF_0.9 minus CNTL. (a), (d) ANN denotes the annual mean. (b), (e) JJA denotes the summer (June–July–August) mean. (c), (f) DJF denotes the winter (December–January–February) mean.

In parallel with CUHI and SUHI, transient albedo also impacts the temporal pattern of urban heat stress indices, as seen in Figure 4(a)–(e). These indices follow the rising trend of atmospheric forcing over the study period, highlighted in Figure C1. The comparison between ROOF_0.9 and CNTL reveals annual-mean reductions in heat stress indices: NWS_HI by $0.6\pm0.007$°C, AT by $0.4\pm0.003$°C, SWBGT by $0.3\pm0.002$°C, HUMIDEX by $0.5\pm0.004$°C, and DI by $0.3\pm0.003$°C. These findings indicate that a higher albedo mitigates the rate at which these indices reach critical thresholds. For instance, NWS_HI in the CNTL and ROOF_DA simulations hit the caution threshold (27°C) in 2043 JJA, nearing the end of the near-term period. In contrast, in the ROOF_0.9 simulation, NWS_HI does not reach the caution threshold until the summer of 2050 (27.1°C), delaying the occurrence by 7 years compared to the CNTL simulation (Figure 4(a)). Meanwhile, the ROOF_DA simulation shows HUMIDEX exceeding the 27°C threshold by 2036 JJA, 6 years later than in the CNTL simulation yet 4 years before the ROOF_0.9 simulation, depicted in Figure 4(d). Regarding the DI, more than half of the population experiences heat discomfort from 2080 onwards in the CNTL simulation. Implementing a 0.9 roof albedo in both ROOF_0.9 and ROOF_DA simulations delays reaching this upper discomfort threshold by 4 years, as shown in Figure 4(e).

Furthermore, indoor air temperature (TBUILD) is influenced by both the background climate changes and modifications to urban roof albedo, as depicted in Figure 4(f). Within the CNTL simulation, the average TBUILD during boreal summer (JJA) crosses the thermal discomfort threshold of 28°C in 2065, escalating to 30.1°C by 2099, marking an increase of 3.7°C over 85 years. Adjusting the roof albedo to 0.9 moderates indoor temperatures, resulting in an annual-mean TBUILD reduction of 1.8±0.02°C when comparing ROOF_0.9 with CNTL. In the ROOF_DA simulation, the gradual increase in roof albedo effectively delays reaching the upper threshold of thermal comfort until 2094, showcasing its long-term benefits. However, a high roof albedo also entails drawbacks for the winter indoor thermal environment. In the CNTL simulation, the mean TBUILD during boreal winter (DJF) remains above the lower comfort threshold of 19°C starting from 2015, suggesting a comfortable indoor temperature in DJF. Conversely, in both ROOF_0.9 and ROOF_DA simulations, DJF mean TBUILD falls below 19°C from 2015 to 2078, necessitating additional heating to maintain DJF thermal comfort (Figure 5(h)).

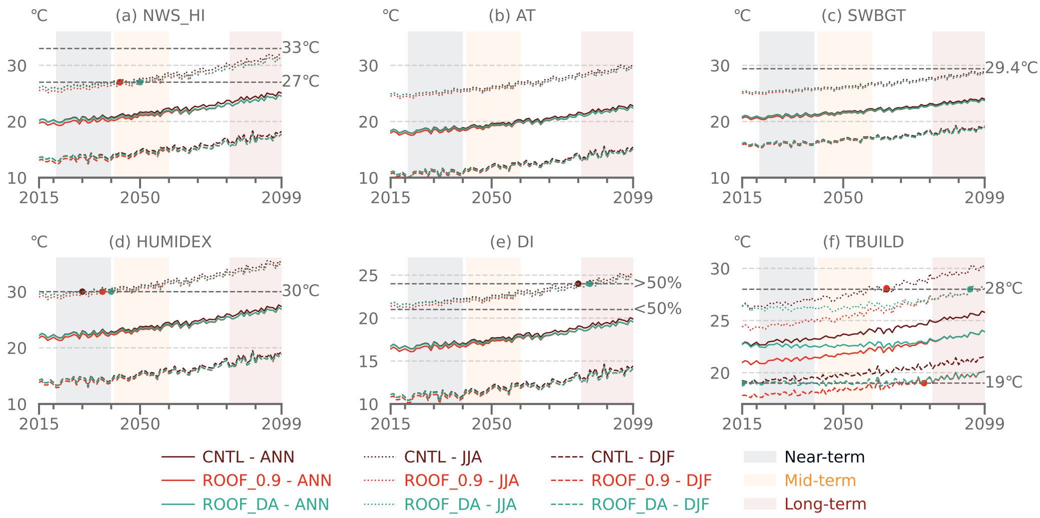


**Figure 4.** Global-mean urban heat stress indices and indoor temperature during 2015–2099 in the CNTL, ROOF_0.9, and ROOF_DA simulations. Referring to Buzan et al. (2015), (a) 2-m US National Weather Service Heat Index (NWS_HI) at 27°C marks the threshold of caution, while at 33°C, it signifies extreme caution. (b) 2-m apparent temperature (AT) lacks a specific description of thresholds. (c) 2-m simplified wet-bulb globe temperature (SWBGT) at 29.4°C indicates caution. (d) 2-m humidity index (HUMIDEX) at 30°C is the threshold of some discomfort. (e) 2-m discomfort index (DI), being unitless, suggests discomfort levels where 21–24 indicates less than half of the population experiencing discomfort and above 24 denotes over half of the population in discomfort. (f) TBUILD is recommended to be within the range of 19–28°C for general activities (Enescu & Flanner, 2017). Dots in (a), (d), (e) and (f) denote the year when reaching thresholds.

### 3.2 The urban surface energy budget responses to roof albedo modifications

Analysis of the urban energy budget, using CNTL, ROOF_0.9, and ROOF_DA simulations, reveals that urban radiation and turbulent fluxes exhibit consistent patterns alongside atmospheric forcing, without large deviation over 85 years (Figure 5(a)–(d)). The CNTL simulation sees urban absorbed solar radiation (FSA) experiencing an annual increase of 0.94%, from 159.88 W $m^{-2}$ in 2015 to 161.38 W $m^{-2}$ in 2099. The FSA rise of 1.50 W $m^{-2}$ is attributed to the FSDS with a similar increase of 1.60 W $m^{-2}$ from 2015 to 2099. Meanwhile, urban net longwave radiation (FIRA) falls by 3.35% to 64.84 W $m^{-2}$, and sensible heat (FSH) rises by 2.1% to 58.3 W $m^{-2}$, with total evaporation (FLH) growing by 6.9% to 40.65 W $m^{-2}$. Building energy consumption adapts to increasing TBUILD due to global warming, influencing heat transfer to the ground and climate system (Figure 5(e)–(i)). Specifically, AC use intensifies from 0.005 W $m^{-2}$ in the summer of 2015 to 0.015 W $m^{-2}$ by the summer of 2099, whereas urban heating demand declines from 0.17 W $m^{-2}$ in the winter of 2015 to 0.13 W $m^{-2}$ by the winter of 2099. As a result, the anthropogenic heat flux (AHF) entering the climate system sees a 28.8% reduction, from 0.081 W $m^{-2}$ to 0.058 W $m^{-2}$, lying above the estimate of 0.059 W $m^{-2}$ by Flanner (2009) but below the 0.15 W $m^{-2}$ by Jin et al. (2019). This discrepancy is likely due to CLMU's building energy model calculating AHF in response to local temperature feedback, in contrast to assessments based on broader energy consumption metrics.

Contrastingly, the introduction of a 0.9 urban roof albedo in the ROOF_0.9 simulation markedly lowers the annual-mean FSA from 159.90±0.96 to 101.24±0.60 W $m^{-2}$, leading to reductions in associated urban heat fluxes, except for AHF. The annual-mean $\Delta$AHF based on ROOF_0.9 minus CNTL simulations is 0.008±0.001 W $m^{-2}$, denoting an additional 0.008±0.001 W $m^{-2}$ AHF directed into the climate system annually, mainly due to an increase in urban heating by 0.0077±0.0008 W $m^{-2}$. The ROOF_DA simulation illustrates the transient response of heat flux to increasing roof albedo, with urban areas absorbing less solar radiation as albedo rises. The annual-mean FSA reduction rate is 0.94±0.0006 W $m^{-2}$ (Tab.B1), with albedo modifications manifesting more distinctly seasonally; the JJA mean FSA reduction is 1.06±0.0008 W $m^{-2}$, while the DJF mean sees a slightly different rate (0.73±0.0008 W $m^{-2}$).

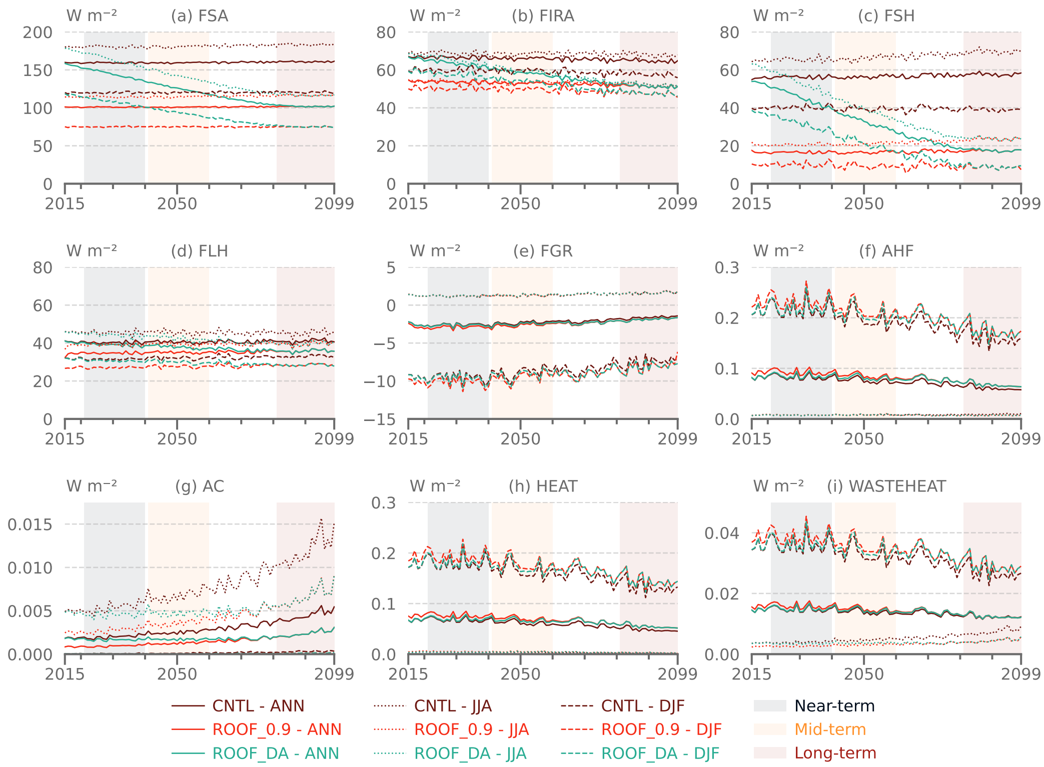


**Figure 5.** Annual-mean grid-level urban energy changes. (a) FSA is the urban absorbed solar radiation. (b) FIRA is the urban net longwave radiation. (c) FSH is the urban sensible heat. (d) FLH is the urban total latent heat. (e) FGR is the urban heat flux into soil/snow. (f) AHF is the anthropogenic heat flux that goes into the climate system. (g) AC is the urban air-conditioning flux. (h) HEAT is the urban heating flux. (i) WASTEHEAT is the sensible heat flux from heating and air-conditioning sources.

### 3.3 Urban land unit and surface heterogeneity with urban albedo modifications

Exploring urban albedo adaptations across urban roofs, impervious roads, and walls underscores the varied impact on urban heat island intensity, urban heat stress, and indoor temperature, with roof albedo modifications showing the most substantial influence. The annual-mean CUHI decrease rates in ROOF_DA, IMPROAD_DA, WALL_DA simulations are $-0.009\pm0.0001$°C, $-0.001\pm0.0005$°C, and $-0.004\pm0.0008$°C, respectively, as shown in Figure 6(a). For SUHI, the decrease rates are $-0.04\pm0.0002$, $-0.003\pm0.0001$, $-0.009\pm0.0002$°C, respectively, highlighted in Figure 6(d). The marginal urban temperature reductions with increased albedo in walls or impervious roads are linked to the marginal decrease in FSA, depicted in Figure B1(a). TBUILD decreases across albedo increases, except in the IMPROAD_DA simulation, where a 0.9 impervious road albedo results in a slight annual-mean TBUILD increase of 0.1°C by 2099 (Figure 6(j)). This rise in indoor temperature, related to the reflectivity of roads, has been reported by Salvati et al. (2022), attributing to the incident diffuse radiation trapped within the urban street canyon.

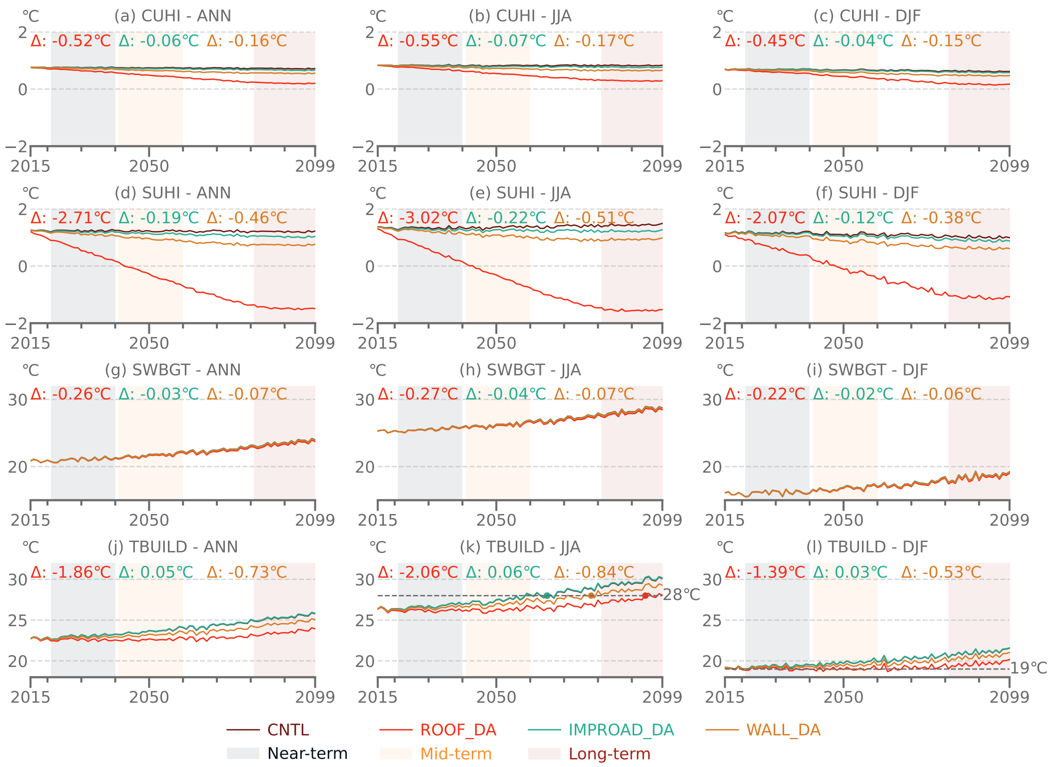


**Figure 6.** Comparisons of global-mean CUHI, SUHI, SWGBT, and TBUILD induced by urban surface albedo changes during 2015–2099. Δ denotes mean ROOF_DA minus CNTL, IMPROAD_DA minus CNTL, and WALL_DA minus CNTL in 2099. (a), (d), (g), (j) ANN denotes the annual mean. (b), (e), (h), (k) JJA denotes the summer mean values during the June–July–August periods. (c), (f), (i), (l) DJF denotes the winter mean values during the December-January-February periods. Dots in (k) denote the year when JJA mean TBUILD reaches the upper threshold of thermal comfort at 28°C.

Comparing urban thermal environments across TBD, HD, and MD areas shows daytime CUHI is more substantially reduced in TBD than in HD and MD (Figure 7). In the CNTL simulation, daytime CUHI averages at 2.0±0.03°C in TBD, compared to 0.7±0.02°C in HD and 0.5±0.02°C in MD. The ROOF_DA simulation induces daytime CUHI reductions of 0.03±0.0002°C in TBD, 0.02±0.0002°C in HD, and 0.01±0.0001°C in MD. Nighttime CUHI exhibits fewer reductions across these density types, although albedo modifications yield the most substantial decreases in TBD. In the WALL_DA simulation, TBUILD shows greater sensitivity in HD, with a 0.9 wall albedo in 2099 leading to a 0.8°C decrease in TBUILD in HD, as opposed to 0.3°C in TBD and 0.7°C in MD.

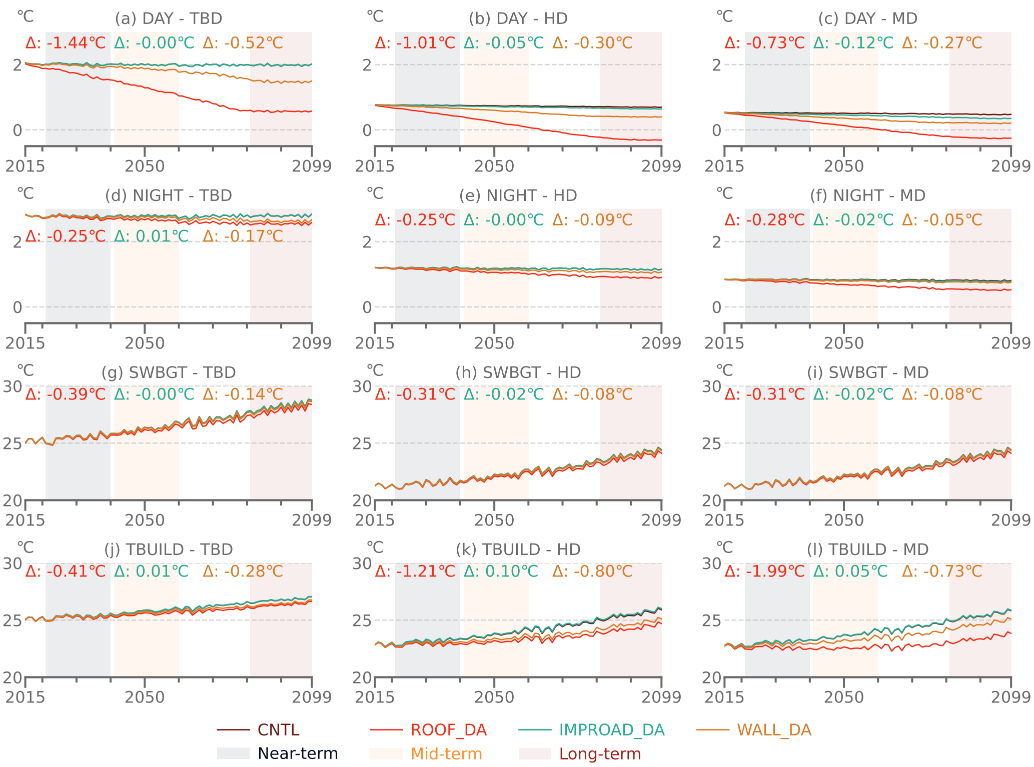


**Figure 7.** Urban land unit heterogeneity during 2015-2099. (a)–(c) DAY denotes the daytime canopy urban heat island (CUHI) by contrasting annual-mean urban and rural daily maximum of average 2-m air temperature. (d)–(f) NIGHT denotes the night CUHI by contrasting the annual-mean urban and rural daily minimum of average 2-m air temperature. (g)–(i) Annual-mean 2-m simplified wet-bulb globe temperature (SWBGT). (j)–(l) Annual-mean indoor temperature (TBUILD). Δ denotes annual-mean ROOF_DA minus CNTL, IMPROAD_DA minus CNTL, and WALL_DA minus CNTL in 2099.

Moreover, simulations combining albedo modifications across urban surface types, ROOF_IMPROAD_DA and ROOF_IMPROAD_WALL_DA, demonstrate compounded effects, with SUHI in 2099 dropping by 2.9°C and 3.7°C, respectively, compared to the CNTL simulation. The SUHI reductions from the ROOF_DA, IMPROAD_DA, and WALL_DA simulations are 2.7°C, 0.2°C, and 0.5°C, respectively. A more pronounced SUHI reduction occurs when high albedo is applied simultaneously to multiple surfaces. Specifically, a 0.01 albedo increment in both roofs and impervious roads in the ROOF_IMPROAD_DA simulation reduces the annual-mean FSA by 1.06 W m$^{-2}$, slightly the 1.27 W m$^{-2}$ change in radiative forcing projected by a similar albedo increase in Akbari et al. (2009). This discrepancy may result from the differences in the FSDS between the two studies, with our simulations showing an FSDS of 193.6±1.1 W m$^{-2}$ compared to the 206 W m$^{-2}$ assumed by Akbari et al. (2009). Additionally, the allocation of urban horizontal surfaces in CLMU, with roofs and impervious roads constituting 44.3% and 15.5%, diverges from Akbari et al. (2009)'s 25% for roofs and 35% for impervious roads, influencing the effects on FSA.

## 4 Implications for urban climate-sensitive design strategies

Our experimental simulations extend beyond previous studies on quantifying the effects of white roofs and cool pavements through global urban climate modelling (Tab. 1), offering insights into albedo-induced adaptation effects in terms of urban heterogeneity, global spatial differences, and seasonal variations. The distinct impacts of modifying albedo on roofs, impervious roads, and walls characterize their potential in future urban design and planning. For instance, a 0.01 increment in roof albedo leads to a 0.94±0.0006 W $m^{-2}$ decrease in FSA, whereas the same increase in impervious road and wall albedo decreases FSA by 0.11±0.0001 W $m^{-2}$ and 0.24±0.0002 W $m^{-2}$, respectively.

The differential impacts highlight the important role of roof albedo modification in lowering urban temperature globally, as opposed to the relatively modest contributions from impervious road and wall albedo modifications. Moreover, special attention should be paid to TBD areas, where thermal conditions pose greater challenges compared to MD and HD areas. Despite the application of high roof albedo, TBD areas are more prone to reaching the discomfort threshold of 30°C. These findings underscore the importance of targeted interventions in densely built-up areas.

Considering the near-term projection that annual-mean NWS_HI and HUMIDEX will surpass the 30°C thermal discomfort threshold around 2030 to 2040, the near-future period, this timeline suggests a critical window for implementing albedo modifications. Spatial analysis of urban temperature reductions reveals pronounced disparities, with lower reductions in low-latitude areas such as South America, the Middle East, and South Asia compared to high latitudes (Figure 8(a)). The JJA mean and DJF mean reduction in urban surface temperature are 1.2±0.5 and 0.9±0.6°C, respectively, highlighting both seasonal and spatial differences. Elevated impervious road albedo is observed to cool certain areas such as Eastern China (Figure 8(d)–(f)), whereas central Europe and Southeast Asia see advantages from increased wall albedo (Figure 8(g)–(i)).

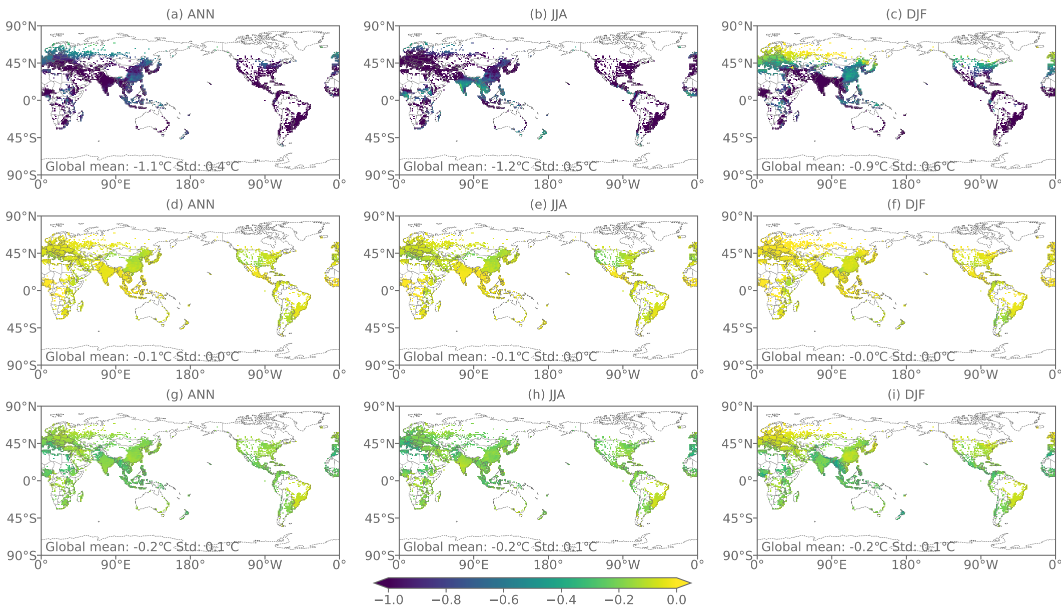


**Figure 8.** Reductions of urban surface temperature (ΔTG_U) in 2040 (the end of near-term). (a)–(c) ROOF_DA minus CNTL. (d)–(f) IMPROAD_DA minus CNTL. (g)–(i) WALL_DA minus CNTL.

The indoor thermal environment emerges as another factor in formulating adaptation strategies involving urban albedo modifications. By 2040, the JJA mean reduction in indoor temperature resulting from the ROOF_DA compared to CNTL simulations is approximately 0.7±0.2°C, similar to the winter (DJF) mean reduction 0.7±0.5°C. When resolved by latitude, urban areas at 42.88°N latitude experience the maximum decrease of JJA mean TBUILD (1.2°C) and urban areas at 49.48°S face the maximum DJF mean TBUILD decrease (2.0°C) (Figure 9(a)–(c)). However, the indoor cooling effects stemming from urban albedo modifications are not globally consistent, particularly in high-latitude regions that face increased demands for heating. In 2040, the annual-mean AC reduces to 0.0009 W m$^{-2}$, a decrease of 0.0003 W m$^{-2}$ from the CNTL simulation. Conversely, the annual mean HEAT increases by 0.002 W m$^{-2}$, nearly ten times more than the AC reductions. The trade-off between cooling efficiency in summer and energy consumption in winter should be particularly considered in the high-latitude regions. Viewed from a long-term perspective, the combined demands for air conditioning and heating in simulations incorporating transient albedo modifications show an upward trend in the urban areas located beyond 30°N and 25°S latitudes (Figure 10).

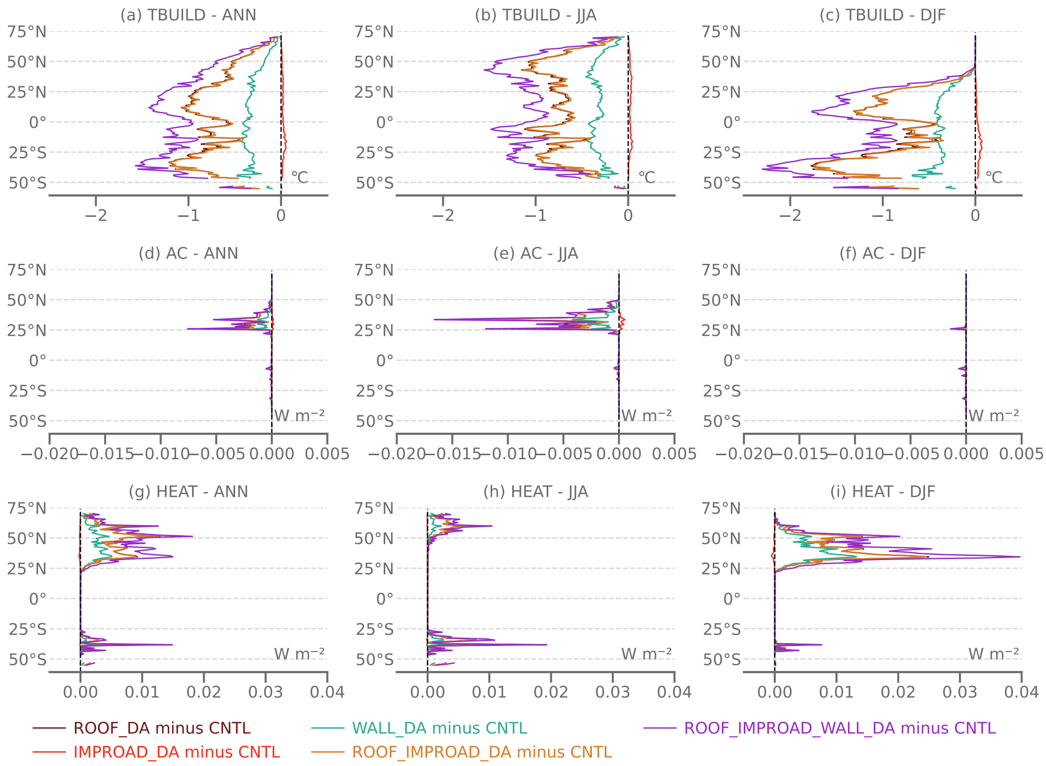


**Figure 9.** Latitude variations of indoor temperature (TBUILD), air conditioning (AC) and heating (HEAT) in 2040 (the end of near-term).

To overcome the constraints associated with static cooling roofs, current innovations are exploring thermotropic materials capable of changing colors from dark to light in response to temperature variations throughout the day or across seasons (Sharma et al., 2017; Ye et al., 2012). The potential for advancing the evaluation of transient material characteristics, employing monthly or even more frequent calculations, is promising within the framework of the transient urban albedo scheme. Architecture designs incorporating cooling envelopes and adaptive materials should proceed with caution, recognizing that high albedo strategies may not be universally applicable. Assessing such strategies should extend beyond the immediate impacts on urban temperature and building energy demands.

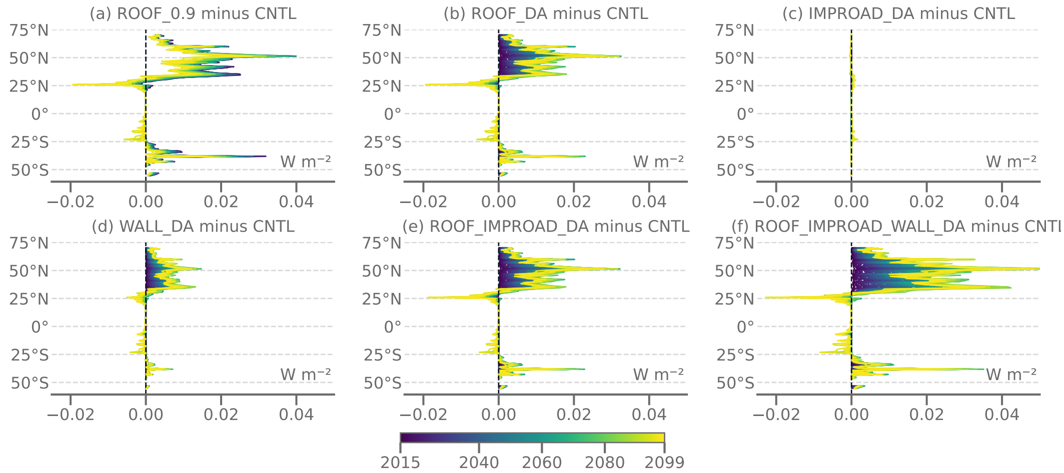


**Figure 10.** Annual-mean air conditioning (AC) plus heating (HEAT) from 2015 to 2099.

## 5 Conclusions

In this study, we developed a new transient urban surface albedo scheme within the Community Earth System Model (CESM) to explore the dynamic nature of urban climate adaptation strategies across urban surfaces including roofs, impervious roads, and walls. This new scheme allows for the evaluation of urban surface albedo modification impacts globally, focusing on urban thermal environments (e.g., urban heat island, urban heat stress, and indoor temperature), the urban energy budget, and the complexity of urban heterogeneity. Our findings underscore that the urban thermal environment, especially the urban absorbed solar radiation, responds to transient urban albedos over time, with roof albedo modifications being notably effective, followed by wall and impervious road albedo modifications. Implementing an annual increase of 0.01 in roof albedo is expected to reduce the annual mean canopy urban heat island from 0.8°C in 2015 to 0.2°C by 2099. Comparisons across ROOF_DA, IMPROAD_DA, and WALL_DA simulations shed light on the role of urban surface heterogeneity in influencing the local urban climate. Furthermore, our findings indicate that higher albedo configurations are especially effective in cooling environments within tall building districts, compared to high and middle-density areas.

The simulations underscore the pressing need for urban heat mitigation, highlighted by the projection that indices such as June–July–August (JJA) mean NWS_HI (National Weather Service Heat Index) and HUMIDEX (2-m humidity index) will surpass critical thresholds by the end of the near-term (2021–2040). Despite practical considerations indicating that urban albedo might not achieve ideal levels as the simulations, this study aims to provide guidance for urban climate-sensitive design and policy development through modifications to urban albedo on a global scale across various time frames. It emphasizes the importance of holistic strategy selection over singular solutions like white roofing, urging consideration of localized factors such as geographical location, urban density types, and surface properties that affect urban albedo's impact on urban thermal environments, energy usage, and overall urban climate.

Acknowledging practical constraints, it is unlikely that urban albedo will reach the ideal value but rather remain at a relatively lower level. This study endeavors to inform the urban climate-sensitive design and adaptive policy-making by assessing the global impacts of changes in urban surfaces. Further examination of these impacts on specific cities should be achieved by employing regional climate models with more explicit urban representation and parameterization in finer resolutions. In the face of uncertain urban climate risks, a transient representation of urban albedo proves beneficial for modelling flexible urban adaptive policy and practice over time. Additionally, this scheme holds promise for applications beyond policy-driven adaptations, such as representing natural variations in albedo due to surface material wear and tear/weathering, pollutant deposition, or changes in vegetation cover. For instance, the albedo of green roof albedo can fluctuate with the growth cycles of vegetation and seasonal changes in leaf cover. The scheme can be adapted to model these dynamic changes by customizing urban albedo adjustments in the corresponding time steps.

As global climate models/Earth system models advance to feature finer grid spacings and higher temporal resolutions, which usually result in increased computational demands, the ability to account for spatiotemporal variations in urban surface albedo becomes increasingly important for projecting local urban climate. Our new scheme for incorporating transient urban surface albedo demonstrates computational efficiency, minimizing additional computational costs, as illustrated in Appendix D. Moreover, this scheme's adaptability is not limited to urban surface albedo modifications but also facilitates incorporating additional urban canopy parameters, such as urban surface emissivity. This expansion offers more options for representing complex urban environments without imposing substantial computational burdens.

# Appendix A Community Earth System Model–Urban (CLMU)

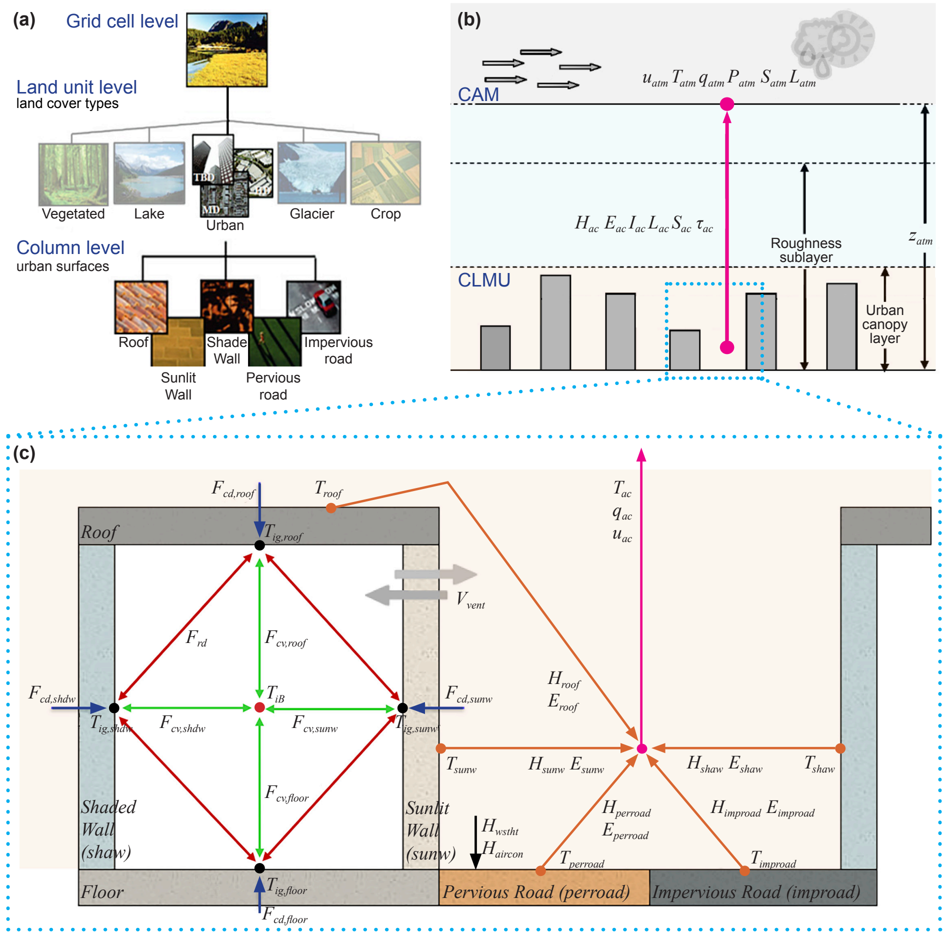


**Figure A1.** Urban representation and parameterization. (a) urban surface representation hierarchy in the CLM. (b) interactions between the atmosphere and urban canopy. CLMU is forced by the CAM at reference height $z_{atm}$ (m). Atmospheric parameters include the atmospheric wind $u_{atm}$ (m s$^{-1}$), temperature $T_{atm}$ (K), humidity $q_{atm}$ (kg kg$^{-1}$), precipitation $P_{atm}$ (mm s$^{-1}$), solar radiation $S_{atm}$ (W m$^{-2}$), and longwave radiation $L_{atm}$ (W m$^{-2}$). The pick arrows represent the upward fluxes from the urban canopy layer to CAM, including sensible heat flux $H_{ac}$ (W m$^{-2}$), water vapour flux $E_{ac}$ (kg m$^{-2}s^{-1}$), albedo $I_{ac}$, emitted longwave radiation $L_{ac}$ (W m$^{-2}$), absorbed short-wave $S_{ac}$ (W m$^{-2}$), and momentum $\tau_{ac}$ (kg m$^{-1}$ $s^{-2}$). (c) urban energy scheme. $T_{ac}$ is the urban canopy air temperature (K), $q_{ac}$ the specific humidity of urban canopy layer air (kg kg$^{-1}$), and $u_{ac}$ the wind speed (m s$^{-1}$) at the average height of the building. The orange arrows represent the heat and moisture fluxes (W m$^{-2}$) from the urban facets to the §urban canopy air. $T_{roof}$, $T_{sunw}$, $T_{shaw}$, $T_{perroad}$, and $T_{improad}$ is the surface temperature of the roof, sunlit wall, shaded wall, pervious surfaces, and impervious surfaces. $H_{roof}$, $H_{sunw}$, $H_{shaw}$, $H_{perroad}$, and $H_{improad}$ is the sensible heat flux on each surface. $E_{roof}$, $E_{sunw}$, $E_{shaw}$, $E_{perroad}$, and $E_{improad}$ is the water vapor flux. Blue arrows represent heat conduction fluxes (W m$^{-2}$) of the roof $F_{cd,roof}$, sunlit wall $F_{cd,sunw}$, shaded wall $F_{cd,shaw}$, and floor $F_{cd,floor}$. The red arrows represent longwave exchange $F_{rd}$ (W m$^{-2}$) between the interior surfaces. Green arrows represent sensible heat transfer (W m$^{-2}$) between the interior surface of the building and the indoor air by $F_{cv,roof}$, $F_{cv,sunw}$, $F_{cv,shaw}$, and $F_{cv,floor}$, respectively. The black arrows represent the heat waste $H_{wstht}$ (W m$^{-2}$) and the heat removed $H_{aircon}$ (W m$^{-2}$) by air conditioning. Grey arrows represent the ventilation flow rate $V_{\rm vent}$ (m$^3s^{-1}$). Source: Adapted from Oleson et al. (2013); Oleson and Feddema (2020).

# Appendix B Urban albedo-induced energy changes

**Table B1.** Statistical regression between annual-mean absorbed solar radiation and ALB using the fixed effect model.

| Simulation | ROOF_DA | ROOF_DA | ROOF_DA | IMPROAD_DA | WALL_DA | ROOF_IMPROAD_DA | ROOF_WALL_IMPROAD_DA |
|---|---|---|---|---|---|---|---|
| Variable metric | ANN | JJA | DJF | ANN | ANN | ANN | ANN |
| Dependent variable | FSA | | | | | | |
| ALB | $-94.096^{***}$ | $-105.70^{***}$ | $-73.135^{***}$ | $-11.370^{***}$ | $-24.312^{***}$ | $-105.80^{***}$ | $-139.74^{***}$ |
| FSDS | $0.7204^{***}$ | $0.6914^{***}$ | $0.6740^{***}$ | $0.8050^{***}$ | $0.7586^{***}$ | $0.6957^{***}$ | $0.5962^{***}$ |
| Constant | $46.611^{***}$ | $58.817^{***}$ | $41.927^{***}$ | $7.2874^{***}$ | $19.487^{***}$ | $54.754^{***}$ | $84.352^{***}$ |
| Number of grid cells with urban fraction | 3538 | | | | | | |
| Adjusted $r^2$ | 0.866 | 0.857 | 0.732 | 0.926 | 0.898 | 0.887 | 0.932 |

Note: ANN denotes the annual mean, JJA denotes the June–July–August mean, DJF denotes the December–January–February mean. *** denotes the significance at 1% significance level.

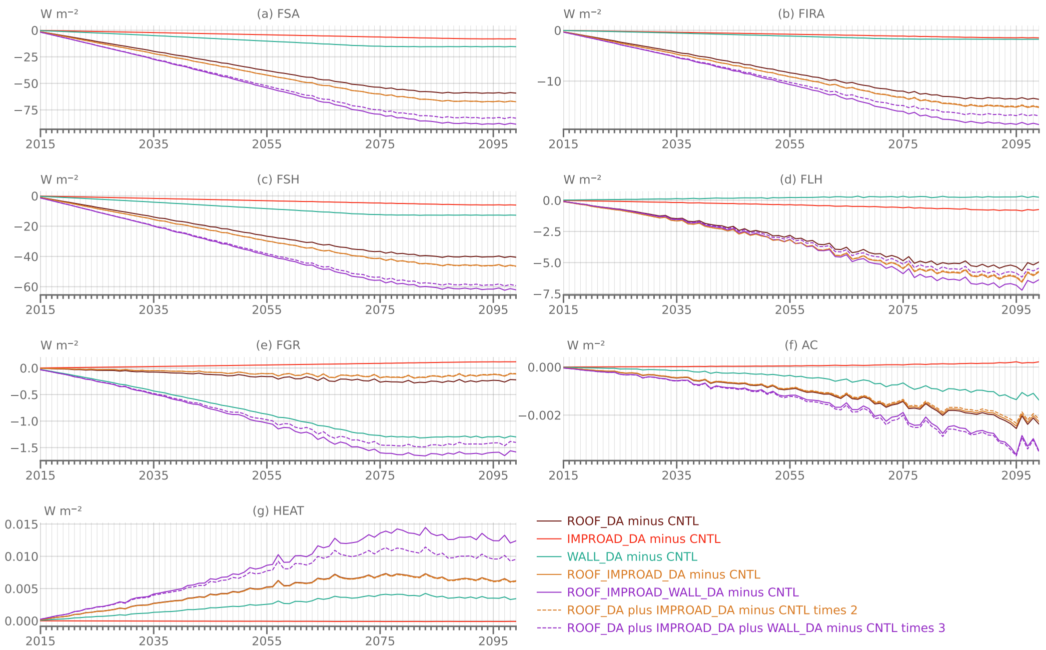


**Figure B1.** Urban heat flux changes induced by transient urban albedo.

# Appendix C Atmospheric variables

This study uses atmosphere data from the BSSP370cmip6 simulations. As shown in the period 2015–2099 (Figure C1), the annual mean TBOT jumps from 18.2°C in 2015 to 18.9°C in 2050 and 21.7°C in 2099. Seasonally, in the June–July–August (JJA) period, TBOT reaches 27.2°C in 2099, 3.1°C and 3.8°C higher than in 2050 and 2015, respectively. In the December–January–February (DJF) period, TBOT shows a 3.2°C increase over 85 years. FLDS and QBOT show a similar trend of accelerating growth as TBOT. FSDS and PBOT fluctuate moderately while rainfall displays intensive changes, particularly in summer. Alongside warming, snowfall generally reduces.

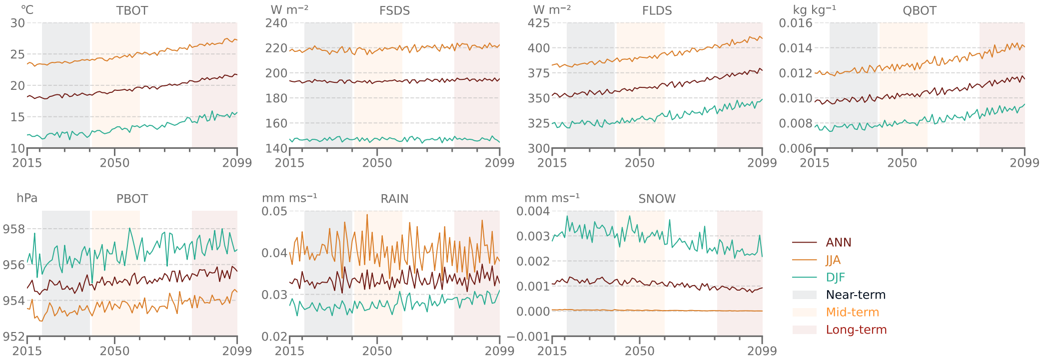


**Figure C1.** Period (2015–2099) of atmospheric variables under the SSP3-7.0 scenario. Atmospheric variables are calculated for annual-mean, June–July–August (JJA) mean, and December–January–February (DJF) mean. TBOT is the atmospheric air temperature (°C). FSDS is the atmospheric incident solar radiation (W m$^{-2}$). FLDS is the longwave radiation (W m$^{-2}$). QBOT is the specific humidity (kg kg$^{-1}$). PBOT is the surface pressure (hPa). RAIN is the rain (mm ms$^{-1}$). SNOW is the snow (mm ms$^{-1}$).

Given land-only simulations, the two-way interactions between urban and atmosphere are excluded except for urban-to-atmosphere feedback. Simulation outputs of atmospheric variables overlap and are presented as a single line in each subplot (Figure C2), which indicates that atmospheric variables in all cases are the same.

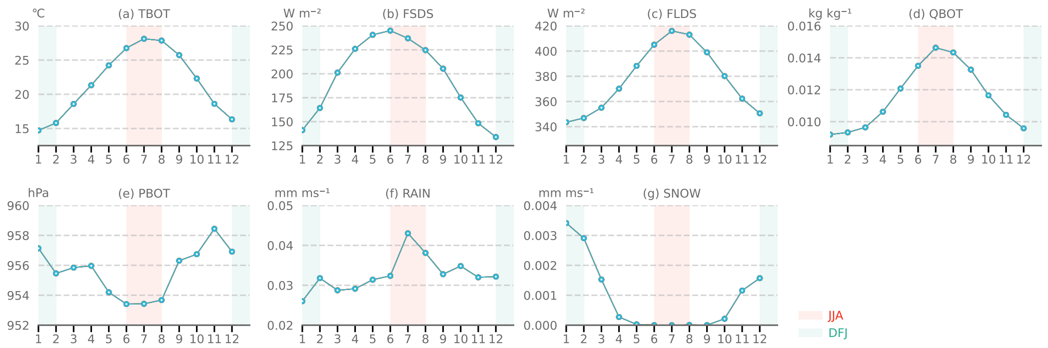


**Figure C2.** Global-averaged monthly mean atmospheric variables in 2099. Data are collected from those land grids that contain urban fractions in CLM. Atmospheric variables are calculated for their global monthly mean in 2099 under the SSP3-7.0 scenario. They show seasonal fluctuation in a year, particularly in the June–July–August (JJA) and December-January-February (DJF) periods.

## Appendix D Workflow profiling

We used the UK National Supercomputing Service named ARCHER2 (`https://docs.archer2.ac.uk/user-635guide/hardware/`) to evaluate the computational performance of the transient urban albedo scheme in CESM2.1.4. In ARCHER2, each computer node has 128 cores as dual AMD EPYC 7742 64-core 2.25GHz processing elements (PEs). The compiler is the GNU Compiler Collection, the MPI library is MPICH, and the model driver is CPL7. The component set includes a data atmosphere component (DATM), active land component (CLM5), and active river runoff component (MOSART) with other stub components such as glacier (GLC), sea-ice (ICE), surface wave (WAV), and ocean (OCN). We evaluated the computational performance of the new scheme from two aspects: workflow and cost.

Based on a single node of 128 cores, we compared workflows using default and transient schemes through 3-year simulations from 2015–2018. A conventional branch approach with the default scheme needed to manually resubmit case by case to realize albedo input varying by time (Figure D1(a)). Using the transient urban albedo scheme read in data streams without interruptions, where the simulation spent 0.8 min for initialization, 79.2 min for job running, and 0.5 min for output archive (Figure D1(b)). Both the branch approach and stream approach cost similar computing resources of 56.2–56.7 pe-hrs/simulated_year, whose final outputs are almost the same.

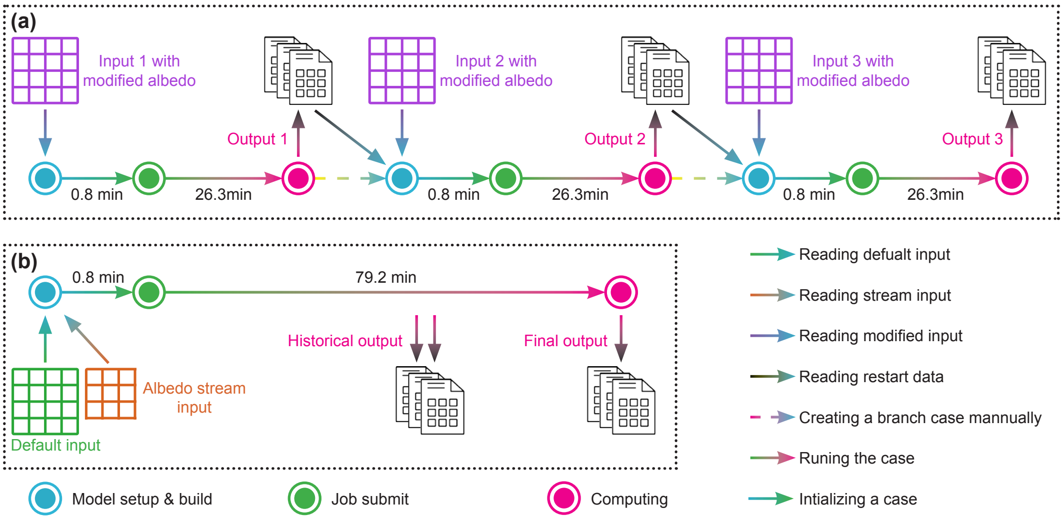


**Figure D1.** Workflows of implementing time-varying urban surface albedos. (a) default scheme, (b) transient urban albedo scheme. Both simulations ran from 2015 to 2018 using 1 node/128 total PEs in the Archer2 machine.

To examine computational cost, we ran land-only simulations with a grid spacing of 0.9° latitude by 1.25° longitude for 20 years from 2015 to 2035 without any half-stopping or re-submission. We set several task configurations: single (1 node/128 total PEs), small (4 nodes/12 total PEs, and 6 nodes/768 total PEs), medium (8 nodes/1024 total PEs), large (12 nodes/1536 total PEs), and heavy (16 nodes/2048 total PEs) task counts. Each configuration ran two simulations: one used the default scheme (Dynamic_UrbanAlbedoRoof = .false.) and the other used the transient urban albedo scheme (Dynamic_UrbanAlbedoRoof = .true.). The major difference between the two schemes was the land model process, where the machine read and calculated roof albedo whether by constant parameters or data streams. The simulation timing was recorded through CESM's tool 'getTiming'.

Figure D2 shows computational cost, initialization time, and run speed. Those employing the transient urban albedo scheme closely match the default scheme in terms of computational cost and overall simulation speed. Though the overall difference is relatively minimal, the transient scheme exhibited a longer initialization period in the 1-node and 4-node simulations.

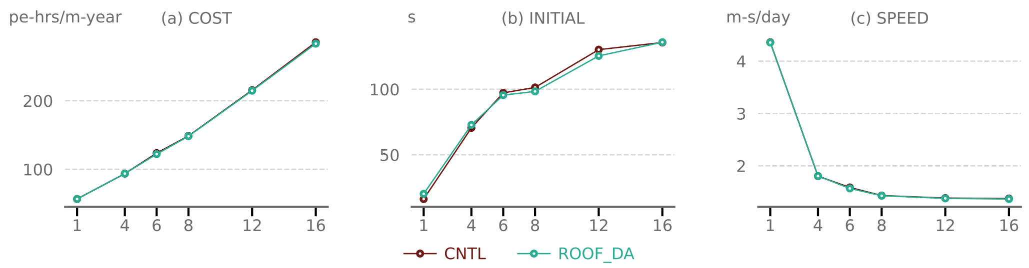


**Figure D2.** Profiling of different simulation workflows. (a) COST denotes computation cost, measured in processing element hours per simulated year. (b) INITIAL denotes the model initialization time, measured in seconds. (c) SPEED denotes the simulation running speed, measured in a simulated year per wall day.

# Appendix E Abbreviations and acronyms

**Table E1.** Variable definitions.

| Variable name | Long name description | Unit | Data source |
|---|---|---|---|
| AC* | Air conditioning | W m$^{-2}$ | CLM outputs |
| AHF | Anthropogenic heat flux going into climate system | W m$^{-2}$ | Eqn. 9 |
| ALB | Land-unit averaged urban surface albedo | unitless | Eqn. 11 |
| AT | 2-m apparent temperature | °C | CLM outputs |
| CUHI | Canopy air urban heat island intensity | °C | Eqn. 2 |
| DI | 2-m discomfort index | unitless | CLM outputs |
| FGR* | Urban ground heat flux | W m$^{-2}$ | CLM outputs |
| FIRA* | Urban net longwave radiation | W m$^{-2}$ | CLM outputs |
| FLDS* | Atmospheric longwave radiation | W m$^{-2}$ | CLM outputs |
| FLH | Urban latent heat flux | W m$^{-2}$ | CLM outputs |
| FSA* | Urban absorbed solar radiation | W m$^{-2}$ | CLM outputs |
| FSDS* | Atmospheric incident solar radiation | W m$^{-2}$ | CLM outputs |
| FSH* | Urban sensible heat flux | W m$^{-2}$ | CLM outputs |
| HEAT* | Building space heating | W m$^{-2}$ | CLM outputs |
| HUMIDEX* | 2-m humidity index | °C | CLM outputs |
| NWS_HI | 2-m US National Weather Service Heat Index | °C | CLM outputs |
| QBOT* | Atmospheric humidity | kg kg$^{-1}$ | CLM outputs |
| RAIN* | Rain | mm ms$^{-1}$ | CLM outputs |
| SNOW* | Snow | mm ms$^{-1}$ | CLM outputs |
| SUHI | Surface urban heat island intensity | °C | Eqn. 1 |
| SWBGT* | 2-m simplified wet-bulb globe temperature | °C | CLM outputs |
| TBOT* | Atmospheric air temperature | °C | CLM outputs |
| TBUILD* | Indoor temperature | °C | CLM outputs |
| TG_R* | Rural surface temperature | °C | CLM outputs |
| TG_U* | Urban surface temperature | °C | CLM outputs |
| TSA_R* | Rural 2-m air temperature | °C | CLM outputs |
| TSA_U* | Urban 2-m air temperature | °C | CLM outputs |
| WASTEHEAT* | Sensible heat flux from heating and cooling sources of urban waste heat | W m$^{-2}$ | CLM outputs |

Note: * denotes using variable names along with the corresponding CLM output variables.

# Open Research

The source code of UrbanDynAlbMod scheme, as well as the scripts and data to reproduce the results and figures, are available at `https://github.com/envdes/code_DynamicUrbanAlbedo` or DOI: 10.5281/zenodo.10903399.

## Acknowledgments

This work used the ARCHER2 UK National Supercomputing Service (`https://www.archer2.ac.uk`). The authors would like to acknowledge the assistance given by Research IT and the use of the HPC Pool and Computational Shared Facility at The University of Manchester. The support of Dr. Douglas Lowe and Christopher Grave from Research IT at The University of Manchester is gratefully acknowledged. Z.Z. appreciates the support provided by the academic start-up funds from the Department of Earth and Environmental Sciences at The University of Manchester. Y.S. is supported by Z.Z's academic start-up funds. Contributions from K.W.O. are based upon work supported by the NSF National Center for Atmospheric Research, which is a major facility sponsored by the U.S. National Science Foundation under Cooperative Agreement No. 1852977. The authors declare no conflict of interest.

## References

Akbari, H., & Matthews, H. D. (2012). Global cooling updates: Reflective roofs and pavements. *Energy and Buildings*, *55*, 2–6. doi: 10.1016/j.enbuild.2012.02.055

Akbari, H., Matthews, H. D., & Seto, D. (2012). The long-term effect of increasing the albedo of urban areas. *Environmental Research Letters*, *7*(2), 024004. doi: 10.1088/1748-9326/7/2/024004

Akbari, H., Menon, S., & Rosenfeld, A. (2009). Global cooling: Increasing world-wide urban albedos to offset $CO_2$. *Climatic Change*, *94*(3-4), 275–286. doi: 10.1007/s10584-008-9515-9

Biardeau, L. T., Davis, L. W., Gertler, P., & Wolfram, C. (2020). Heat exposure and global air conditioning. *Nature Sustainability*, *3*(1), 25–28. doi: 10.1038/s41893-019-0441-9

Boriboonsomsin, K., & Reza, F. (2007). Mix design and benefit evaluation of high solar reflectance concrete for pavements. *Transportation Research Record*, *2011*(1), 11–20. doi: 10.3141/2011-02

Buzan, J. R., Oleson, K. W., & Huber, M. (2015). Implementation and comparison of a suite of heat stress metrics within the Community Land Model version 4.5. *Geoscientific Model Development*, *8*(2), 151–170. doi: 10.5194/gmd-8-151-2015

Chakraborty, TC., Lee, X., Ermida, S., & Zhan, W. (2021). On the land emissivity assumption and Landsat-derived surface urban heat islands: A global analysis. *Remote Sensing of Environment*, *265*, 112682. doi: 10.1016/j.rse.2021.112682

Chen, J., Zhou, Z., Wu, J., Hou, S., & Liu, M. (2019). Field and laboratory measurement of albedo and heat transfer for pavement materials. *Construction and Building Materials*, *202*, 46–57. doi: 10.1016/j.conbuildmat.2019.01.028

Dirmeyer, P. A., Gao, X., Zhao, M., Guo, Z., Oki, T., & Hanasaki, N. (2006). GSWP-2: Multimodel analysis and implications for our perception of the land surface. *Bulletin of the American Meteorological Society*, *87*(10), 1381–1398. doi: 10.1175/BAMS-87-10-1381

Djukic, A., Vukmirovic, M., & Stankovic, S. (2016). Principles of climate sensitive urban design analysis in identification of suitable urban design proposals. Case study: Central zone of Leskovac competition. *Energy and Buildings*, *115*, 23–35. doi: 10.1016/j.enbuild.2015.03.057

Du, H., Zhan, W., Liu, Z., Li, J., Li, L., Lai, J., … Jiang, S. (2021). Simultaneous investigation of surface and canopy urban heat islands over global cities. *ISPRS Journal of Photogrammetry and Remote Sensing*, *181*, 67–83. doi: 10.1016/j.isprsjprs.2021.09.003

Dursun, D., & Yavas, M. (2015). Climate-sensitive urban design in cold climate zone: The city of erzurum, turkey. *International Review for Spatial Planning and Sustainable Development*, *3*(1), 17–38. doi: 10.14246/irspsd.3.1_17

Enescu, D., & Flanner, M. G. (2017). A review of thermal comfort models and indicators for indoor environments. *Renewable and Sustainable Energy Reviews*, *79*, 1353–1379. doi: 10.1016/j.rser.2017.05.175

Epstein, Y., & Moran, D. S. (2006). Thermal comfort and the heat stress Indices. *Industrial Health*, *44*(3), 388–398. doi: 10.2486/indhealth.44.388

Erell, E., Pearlmutter, D., Boneh, D., & Kutiel, P. B. (2014). Effect of high-albedo materials on pedestrian heat stress in urban street canyons. *Urban Climate*, *10*, 367–386. doi: 10.1016/j.uclim.2013.10.005

Flanner, M. G. (2009). Integrating anthropogenic heat flux with global climate models. *Geophysical Research Letters*, *36*(2). doi: 10.1029/2008GL036465

Gao, J., & O'Neill, B. C. (2020). Mapping global urban land for the 21st century with data-driven simulations and Shared Socioeconomic Pathways. *Nature Communications*, *11*(1), 2302. doi: 10.1038/s41467-020-15788-7

Georgescu, M., Morefield, P. E., Bierwagen, B. G., & Weaver, C. P. (2014). Urban adaptation can roll back warming of emerging megapolitan regions. *Proceedings of the National Academy of Sciences*, *111*(8), 2909–2914. doi: 10.1073/pnas.1322280111

Guo, T., He, T., Liang, S., Roujean, J.-L., Zhou, Y., & Huang, X. (2022). Multidecadal analysis of high-resolution albedo changes induced by urbanization over contrasted Chinese cities based on Landsat data. *Remote Sensing of Environment*, *269*, 112832. doi: 10.1016/j.rse.2021.112832

Hertwig, D., Ng, M., Grimmond, S., Vidale, P. L., & McGuire, P. C. (2021). High-resolution global climate simulations: Representation of cities. *International Journal of Climatology*, *41*(5), 3266–3285. doi: 10.1002/joc.7018

Hou, H., Su, H., Yao, C., & Wang, Z.-H. (2023). Spatiotemporal patterns of the impact of surface roughness and morphology on urban heat island. *Sustainable Cities and Society*, *92*, 104513. doi: 10.1016/j.scs.2023.104513

Intergovernmental Panel on Climate Change (IPCC). (2023). *Climate change 2021 – The physical science basis* (1st ed.). Cambridge University Press. doi: 10.1017/9781009157896

Jackson, T. L., Feddema, J. J., Oleson, K. W., Bonan, G. B., & Bauer, J. T. (2010). Parameterization of urban characteristics for global climate modeling. *Annals of the Association of American Geographers*, *100*(4), 848–865. doi: 10.1080/00045608.2010.497328

Jacobson, M. Z., & Ten Hoeve, J. E. (2012). Effects of urban surfaces and white roofs on global and regional climate. *Journal of Climate*, *25*(3), 1028–1044. doi: 10.1175/JCLI-D-11-00032.1

Jamei, Y., Rajagopalan, P., & Sun, Q. C. (2019). Spatial structure of surface urban heat island and its relationship with vegetation and built-up areas in Melbourne, Australia. *Science of The Total Environment*, *659*, 1335–1351. doi: 10.1016/j.scitotenv.2018.12.308

Jin, K., Wang, F., Chen, D., Liu, H., Ding, W., & Shi, S. (2019). A new global gridded anthropogenic heat flux dataset with high spatial resolution and long-term time series. *Scientific Data*, *6*(1), 139. doi: 10.1038/s41597-019-0143-1

Krayenhoff, E. S., Broadbent, A. M., Zhao, L., Georgescu, M., Middel, A., Voogt, J. A., … Erell, E. (2021). Cooling hot cities: A systematic and critical review of the numerical modelling literature. *Environmental Research Letters*, *16*(5), 053007. doi: 10.1088/1748-9326/abdcf1

Lawrence, D. M., Fisher, R. A., Koven, C. D., Oleson, K. W., Swenson, S. C., Bonan, G., … Zeng, X. (2019). The Community Land Model Version 5: Description of new features, benchmarking, and impact of forcing uncertainty. *Journal of Advances in Modeling Earth Systems*, *11*(12), 4245–4287. doi: 10.1029/2018MS001583

Li, X., Melaas, E., Carrillo, C. M., Ault, T., Richardson, A. D., Lawrence, P., … Young, A. M. (2022). A comparison of land surface phenology in the northern hemisphere derived from satellite remote sensing and the Community Land Model. *Journal of Hydrometeorology*, *23*(6), 859–873. doi: 10.1175/JHM-D-21-0169.1

Liao, W., Hong, T., & Heo, Y. (2021). The effect of spatial heterogeneity in urban morphology on surface urban heat islands. *Energy and Buildings*, *244*, 111027. doi: 10.1016/j.enbuild.2021.111027

Liu, Y., Chu, C., Zhang, R., Chen, S., Xu, C., Zhao, D., … Cao, Z. (2024). Impacts of high-albedo urban surfaces on outdoor thermal environment across morphological contexts: A case of Tianjin, China. *Sustainable Cities and Society*, *100*, 105038. doi: 10.1016/j.scs.2023.105038

Lopez-Cabeza, V. P., Alzate-Gaviria, S., Diz-Mellado, E., Rivera-Gomez, C., & Galan-Marin, C. (2022). Albedo influence on the microclimate and thermal comfort of courtyards under Mediterranean hot summer climate conditions. *Sustainable Cities and Society*, *81*, 103872. doi: 10.1016/j.scs.2022.103872

Masson, V. (2000). A Physically-Based Scheme For The Urban Energy Budget In Atmospheric Models. *Boundary-Layer Meteorology*, *94*(3), 357–397. doi: 10.1023/A:1002463829265

Masterton, J. M., & Richardson, F. (1979). *Humidex: A method of quantifying human discomfort due to excessive heat and humidity.* Environment Canada, Atmospheric Environment.

Menon, S., Akbari, H., Mahanama, S., Sednev, I., & Levinson, R. (2010). Radiative forcing and temperature response to changes in urban albedos and associated CO2 offsets. *Environmental Research Letters*, *5*(1), 014005. doi: 10.1088/1748-9326/5/1/014005

Oke, T. R. (1987). *Boundary Layer Climates* (2nd ed.). London: Routledge. doi: 10.4324/9780203407219

Oleson, K. W., Bonan, G. B., & Feddema, J. (2010). Effects of white roofs on urban temperature in a global climate model. *Geophysical Research Letters*, *37*(3). doi: 10.1029/2009GL042194

Oleson, K. W., & Feddema, J. (2020). Parameterization and surface data improvements and new capabilities for the community land model urban (CLMU). *Journal of Advances in Modeling Earth Systems*, *12*(2), e2018MS001586. doi: 10.1029/2018MS001586

Oleson, K. W., Lawrence, D. M., Bonan, G. B., Drewniak, B., Huang, M., Levis, S., … Yang, Z.-L. (2013). *Technical Description of version 4.5 of the Community Land Model (CLM)* (Tech. Rep.). National Center for Atmospheric Research.

Oleson, K. W., Monaghan, A., Wilhelmi, O., Barlage, M., Brunsell, N., Feddema, J., … Steinhoff, D. F. (2015). Interactions between urbanization, heat stress, and climate change. *Climatic Change*, *129*(3), 525–541. doi: 10.1007/s10584-013-0936-8

Ouyang, Z., Sciusco, P., Jiao, T., Feron, S., Lei, C., Li, F., … Chen, J. (2022). Albedo changes caused by future urbanization contribute to global warming. *Nature Communications*, *13*(1), 3800. doi: 10.1038/s41467-022-31558-z

Qian, T., Dai, A., Trenberth, K. E., & Oleson, K. W. (2006). Simulation of Global Land Surface Conditions from 1948 to 2004. Part I: Forcing Data and Evaluations. *Scientific Data*, *7*(5), 953–975. doi: 10.1175/JHM540.1

Riahi, K., van Vuuren, D. P., Kriegler, E., Edmonds, J., O'Neill, B. C., Fujimori, S., … Tavoni, M. (2017). The Shared Socioeconomic Pathways and their energy, land use, and greenhouse gas emissions implications: An overview. *Global Environmental Change*, *42*, 153–168. doi: 10.1016/j.gloenvcha.2016.05.009

Salvati, A., Kolokotroni, M., Kotopouleas, A., Watkins, R., Giridharan, R., & Nikolopoulou, M. (2022). Impact of reflective materials on urban canyon albedo, outdoor and indoor microclimates. *Building and Environment*, *207*, 108459. doi: 10.1016/j.buildenv.2021.108459

Santamouris, M., & Fiorito, F. (2021). On the impact of modified urban albedo on ambient temperature and heat related mortality. *Solar Energy*, *216*, 493–507. doi: 10.1016/j.solener.2021.01.031

Santamouris, M., Synnefa, A., & Karlessi, T. (2011). Using advanced cool materials in the urban built environment to mitigate heat islands and improve thermal comfort conditions. *Solar Energy*, *85*(12), 3085–3102. doi: 10.1016/j.solener.2010.12.023

Senevirathne, D. M., Jayasooriya, V. M., Dassanayake, S. M., & Muthukumaran, S. (2021). Effects of pavement texture and colour on Urban Heat Islands: An experimental study in tropical climate. *Urban Climate*, *40*, 101024. doi: 10.1016/j.uclim.2021.101024

Sharma, M., Whaley, M., Chamberlain, J., Oswald, T., Schroden, R., Graham, A., ... Richey, B. (2017). Evaluation of thermochromic elastomeric roof coatings for low-slope roofs. *Energy and Buildings*, *155*, 459–466. doi: 10.1016/j.enbuild.2017.09.030

Steadman, R. G. (1979). The assessment of sultriness. Part I: A temperature-humidity index based on human physiology and clothing science. *Journal of Applied Meteorology*, *18*(7), 861–873. doi: 10.1175/1520-0450(1979)018⟨0861:TAOSPI⟩2.0.CO;2

Steadman, R. G. (1994). Norms of apparent temperature in Australia. *Australian Meteorological Magazine*, *43*, 1–16.

Stull, R. (2011). Wet-Bulb Temperature from Relative Humidity and Air Temperature. *Journal of Applied Meteorology and Climatology*, *50*(11), 2267–2269. doi: 10.1175/JAMC-D-11-0143.1

Tuholske, C., Caylor, K., Funk, C., Verdin, A., Sweeney, S., Grace, K., ... Evans, T. (2021). Global urban population exposure to extreme heat. *Proceedings of the National Academy of Sciences*, *118*(41), e2024792118. doi: 10.1073/pnas.2024792118

Wang, L., Sun, T., Zhou, W., Liu, M., Li, D., Tarasova, M. A., ... Stepanenko, V. M. (2023). Deciphering the sensitivity of urban canopy air temperature to anthropogenic heat flux with a forcing-feedback framework. *Environmental Research Letters*, *18*(9), 094005. doi: 10.1088/1748-9326/ace7e0

Willett, K. M., & Sherwood, S. (2012). Exceedance of heat index thresholds for 15 regions under a warming climate using the wet-bulb globe temperature. *International Journal of Climatology*, *32*(2), 161–177. doi: 10.1002/joc.2257

Wu, S., Lin, X., Bian, Z., Lipson, M., Lafortezza, R., Liu, Q., ... Chen, B. (2024). Satellite observations reveal a decreasing albedo trend of global cities over the past 35 years. *Remote Sensing of Environment*, *303*, 114003. doi: 10.1016/j.rse.2024.114003

Xu, X., Swei, O., Xu, L., Schlosser, C. A., Gregory, J., & Kirchain, R. (2020). Quantifying Location-Specific Impacts of Pavement Albedo on Radiative Forcing Using an Analytical Approach. *Environmental Science & Technology*, *54*(4), 2411–2421. doi: 10.1021/acs.est.9b04556

Yang, J., Wang, Z.-H., & Kaloush, K. E. (2015). Environmental impacts of reflective materials: Is high albedo a 'silver bullet' for mitigating urban heat island? *Renewable and Sustainable Energy Reviews*, *47*, 830–843. doi: 10.1016/j.rser.2015.03.092

Ye, X., Luo, Y., Gao, X., & Zhu, S. (2012). Design and evaluation of a thermochromic roof system for energy saving based on poly(N-isopropylacrylamide) aqueous solution. *Energy and Buildings*, *48*, 175–179. doi: 10.1016/j.enbuild.2012.01.024

Zeng, P., Zong, C., Duan, Z., & Wei, X. (2023). Exploring the spatial interplay between built-up environments and surface urban heat island phenomena in the main urban area of Shanghai. *Energy and Buildings*, *301*, 113739. doi: 10.1016/j.enbuild.2023.113739

Zhang, J., Zhang, K., Liu, J., & Ban-Weiss, G. (2016). Revisiting the climate impacts of cool roofs around the globe using an Earth system model. *Environmental Research Letters*, *11*(8), 084014. doi: 10.1088/1748-9326/11/8/084014

Zhao, L., Lee, X., & Schultz, N. M. (2017). A wedge strategy for mitigation of urban warming in future climate scenarios. *Atmospheric Chemistry and Physics*, *17*(14), 9067–9080. doi: 10.5194/acp-17-9067-2017

Zhao, L., Lee, X., Smith, R. B., & Oleson, K. (2014). Strong contributions of local background climate to urban heat islands. *Nature*, *511*(7508), 216–219. doi: 10.1038/nature13462

Zhao, L., Oleson, K., Bou-Zeid, E., Krayenhoff, E. S., Bray, A., Zhu, Q., ... Oppenheimer, M. (2021). Global multi-model projections of local urban climates. *Nature Climate Change*, *11*(2), 152–157. doi: 10.1038/s41558-020-00958-8

Zheng, Z., Zhao, L., & Oleson, K. W. (2021). Large model structural uncertainty in global projections of urban heat waves. *Nature Communications*, *12*(1), 3736. doi: 10.1038/s41467-021-24113-9